An Evaluation of Ultra-Wideband Propagation Channels

by

R. Jean-Marc Cramer

B.S., Purdue University (1989)
M.S., Purdue University (1991)

Submitted to the Department of Electrical Engineering - Systems
in partial fulfillment of the requirements for the degree of

Doctor of Philosophy

at the

UNIVSERSITY OF SOUTHERN CALIFORNIA

December 2000

Signature of Author . . . .
Department of Electrical Engineering - Systems
23 October, 2000

Certified by . . . .
Robert A. Scholtz
Chairman, Department of Electrical Engineering - Systems
Thesis Supervisor

Certified by . . . .
Keith M. Chugg
Associate Professor
Thesis Supervisor

Certified by . . . .
Peter Baxendale
Professor
Thesis Supervisor

Accepted by . . . .
Robert A. Scholtz
Chairman, Department of Electrical Engineering - Systems

Contents

An Evaluation of Ultra-Wideband Propagation Channels

by

R. Jean-Marc Cramer

Submitted to the Department of Electrical Engineering - Systems
on 23 October, 2000, in partial fulfillment of the
requirements for the degree of
Doctor of Philosophy

Abstract

Ultra-wideband (UWB) communication systems have been proposed for use in a number of different applications where the impulsive nature of the transmitted UWB signals may have advantages over more narrowband communication waveforms. In order to gain a more complete understanding of the potential of UWB communication systems, models describing the UWB propagation channel must be developed. From these models, radio algorithms can be verified, system performance can be predicted and design trades made.

The work presented here consists of two main parts. First techniques appropriate for processing the baseband signals of interest in this work are developed. These algorithms permit evaluation of the incident signal waveform, the angle-of-arrival and the time-of-arrival.

In the second part of this work, the routines are applied to measured data taken at a number of different locations in an office building and the resulting signal information is used to develop models for the UWB indoor propagation channel.

Thesis Supervisor: Robert A. Scholtz
Title: Chairman, Department of Electrical Engineering - Systems

Thesis Supervisor: Keith M. Chugg
Title: Associate Professor

Thesis Supervisor: Peter Baxendale
Title: Professor

Chapter 1

Introduction.

1.1 Motivation and Definitions

Ultra-wideband (UWB) communication systems have been proposed for use in a number of different applications where the impulsive nature of the transmitted UWB signals may have advantages over more narrowband communication waveforms. In order to gain a more complete understanding of the potential of UWB communication systems, models describing the UWB propagation channel must be developed. From these models, radio algorithms can be verified, system performance can be predicted and design trades made.

A bandwidth measure appropriate for UWB signals is the fractional bandwidth B_f, defined as,

$$B_f = 2\frac{f_H - f_L}{f_H + f_L} \tag{1.1}$$

where f_H and f_L are the upper and lower 3 dB points of the signal spectrum, respectively. The Defense Advanced Research Project Agency's (DARPA) Assessment of Ultra-Wideband Radar written in 1990 [9], established a definition for UWB signals as having a fractional bandwidth of greater than 25%. Signals which satisfy this constraint include the baseband Gaussian pulse and the derivative Gaussian pulses employed as signal models in this work, as well as radio-frequency pulses of duration less than four cycles of the carrier waveform. In contrast, narrowband signals are defined to have a fractional bandwidth of less than 1%, and signals with fractional bandwidths between 1% and 25% are termed wideband [56].

The motivation for considering UWB signals for the transmission of information is given by the target applications, some of which require operation in dense multipath and perhaps shadowed environments. In these applications, UWB waveforms may have advantages over more narrowband signals in several respects. First, the fine multipath resolution inherent in the short time-duration pulses can result in reduced signal level fluctuations and hence lower required transmitter power. Second, the UWB signals considered here are baseband; there is no carrier signal involved. This means that the signal energy is concentrated in as low of a frequency range as possible. It is known that electromagnetic signals radiated at lower frequencies tend to have better material penetration properties than signals radiated at higher frequencies. Thus, in a shadowed environment, these UWB waveforms may stand a better chance of propagating sufficient signal energy to maintain a link than a system operating with the same bandwidth, but employing a carrier signal.

Propagation studies and have been reported over channels with smaller fractional bandwidths than those of interest here, for both the indoor and outdoor environments [15], [22], [30], [35], [37], [48], [49], [29]. Most of these studies account for basic parameters, such as the signal power distributions and Doppler spread, and some also include more detailed spatial and temporal information, such as joint angle-of-arrival and time-of-arrival statistics. Given that the transmitted signals for the UWB communication systems of interest here are baseband pulses of approximately one nanosecond in duration, it is possible that the results presented in these references do not completely describe the UWB propagation channel. Further, the fractional bandwidth and the dynamic nature of the received UWB signals preclude many traditional techniques for obtaining spatial information from direct application to the UWB channel characterization problem. Although the radar community has reported work on the scattering characteristics of UWB waveforms [56], research on UWB signal propagation for the purpose of communication channel characterization has not been accomplished. The UWB channel parameters to be characterized in this work include the joint time-of-arrival and angle-of-arrival statistics of the multipath signal components, determined from measured propagation data taken on an array of sensors.

A body of literature has been developed to address the problems of source location and sidelobe reduction for the case of narrowband signals incident on an array of sensors [23], [32]. Wideband techniques have also been reported [4], [16], [21]. Fundamental differences exist between these classical array signal processing techniques, predicated on the incidence of constant envelope signals, and the problem of interest here, where the signals are impulsive in nature. In the narrowband case, as well as the wideband generalizations, an assumption is usually made that each signal-of-interest is present at all sensors at any given moment in time. If these techniques were to be applied to baseband UWB signals, a time window of large enough extent to encompass the incident signal at each sensor in the array would have to be employed. This is accomplished at the expense of time resolution, one of the motivating factors for the use of UWB signals.

Antenna arrays for the processing of UWB signals have been investigated, primarily by the radar community [21], [46], [41], [54], [56]. Array signal processing algorithms for these signals have also been reported [21]. The problems addressed in this work are distinct from those discussed in these references, due to the need to resolve and identify the multipath signal components present in the indoor environment, rather than more isolated radar returns.

The main UWB array signal processing algorithm proposed herein is related to the CLEAN algorithm, first introduced in [19], and well established in the radio astronomy and microwave communities [11], [43], [48], [52], [54], [57] as a non-linear, iterative deconvolution technique. The CLEAN algorithm has also been discussed in the context of relaxation techniques for the solution of elliptic differential equations [10]. Although the CLEAN algorithm has been reported for use on wideband signals [54], the bandwidth in the reported experiment was synthesized by sweeping a tone over a bandwidth of 200 MHz in 2 MHz steps, a smaller bandwidth than that of the UWB waveforms considered here. It has also been previously used in the deconvolution of measured data for communication channel characterization [48], [49], [60], in each case over a smaller bandwidth than that considered here. Application of the CLEAN algorithm to the processing of impulsive UWB waveforms in the time domain has not been previously reported in the available literature, nor has the processing algorithm been applied in a spatio-temporal context on impulsive signals.

Modifications to the CLEAN algorithm were made in order improve the performance on

UWB signals. The original algorithm assumes perfect knowledge of the received signal, something not readily available in the UWB case. It was modified so that an estimate of the received signal could be made and utilized on each iteration. This modified algorithm was called Sensor-CLEAN in order to reflect the fact that the relaxation step was moved from beam-space to sensor-space. Post-processing algorithms were also developed in order to further improve the accuracy and reliability of the signal estimates provided by the Sensor-CLEAN algorithm.

In order to generate spatio-temporal models for the UWB propagation channel, two main tasks were considered in this research. First, the signal processing techniques related to the Sensor-CLEAN algorithm were developed. This permitted the signal arrival information to be extracted from measured propagation data. Second, the recovered signal information was used to create models which describe the propagation of UWB signals in an indoor environment.

1.2 Review of the Multipath Propagation Experiment

A UWB signal propagation experiment was performed by Moe Z. Win in an office building by sounding the channel with an UWB waveform [66]. Signal measurements were made from a fixed impulse transmitter location to receiver locations at 14 different rooms and hallways of the office building, transmitting a pulse train of duty cycle 0.2% and of period of 500 nanoseconds. The building floor plan is shown in Figure 1-1. In each receiver location, measurements were made over a time window of 300 nanoseconds at 49 different points arranged spatially in a fixed-height, 7 sensor $\times$ 7 sensor square grid with 6 inch inter-sensor spacing, covering 3 feet by 3 feet, shown in Figure 1-2. In this figure, θ represents the azimuth look direction. The elevation look angle, ϕ, is measured from a perpendicular to the array. The same absolute delay reference for all recorded profiles was used.

Considering the measured data, samples of the signal received at location P in the building are shown in Figure 1-3, Figure 1-4, and Figure 1-5. This is a relatively high SNR case, and these measurements are from sensors located along a diagonal of the measurement array, at the upper left hand sensor, the middle sensor and the lower right-hand sensor. Further details of the experiment can be found in [66]. Note the arrival of a relatively clean pulse via a line-of-sight (LOS) path, not corrupted by multipath, near the beginning of each trace. The direction-

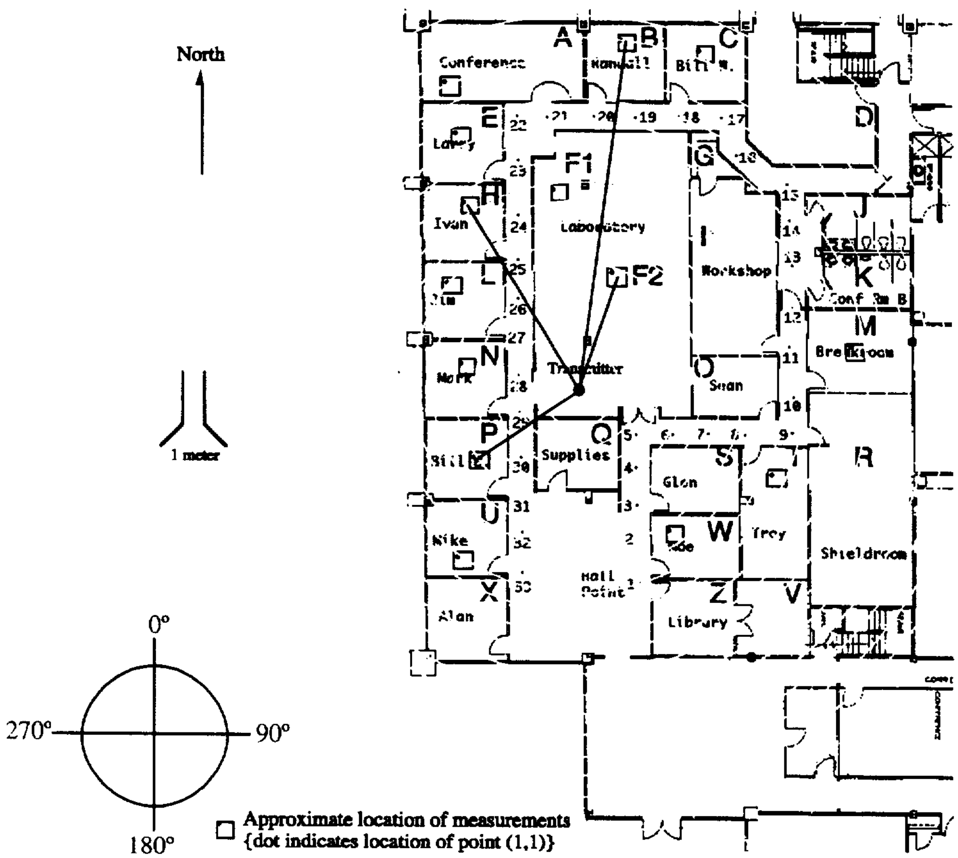

Figure 1-1: Floor plan of building in which experiment was conducted.

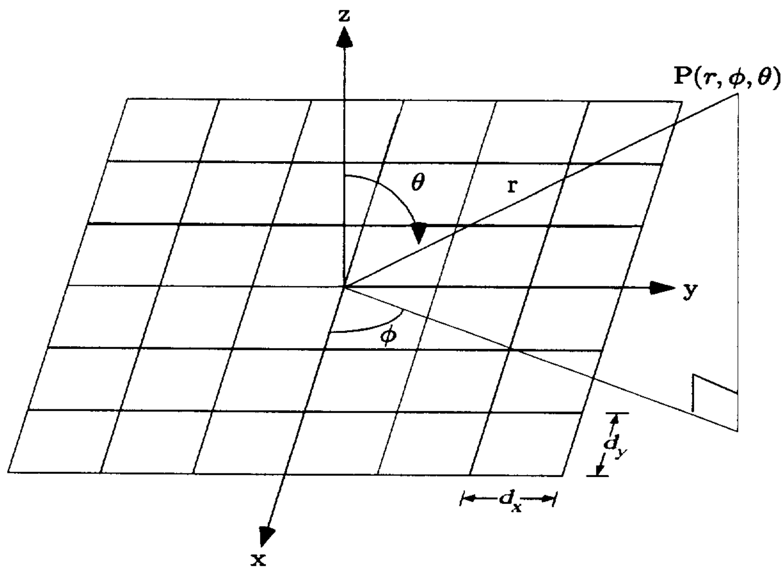

Figure 1-2: Geometry of the measurement array.

of-arrival of this direct path response can be inferred from the time-of-arrival at the sensors, but beyond that, it is difficult to determine much about the angle-of-arrival of the multipath components by inspecting the traces. One of the main goals of this work is to resolve and characterize the time-of-arrival and the angle-of-arrival of these multipath components.

1.3 Representations of the Ultra-Wideband Waveforms

One of the challenges in developing an analytic framework for the study of UWB communication systems is in establishing appropriate signal models. In previous analyses, the signal at the input of the transmit antenna has been modeled as a Gaussian waveform, according to

$$p_0(t) = A_0 \exp\left[-2\pi\left(\frac{t - t_d}{\tau_m}\right)^2\right],$$

where t_d represents the location of the pulse center in time and τ_m is a parameter which determines the temporal width of the pulse. Under this assumption, the ideal transmitted pulse shape, which arrives at the receive antenna can be modeled as

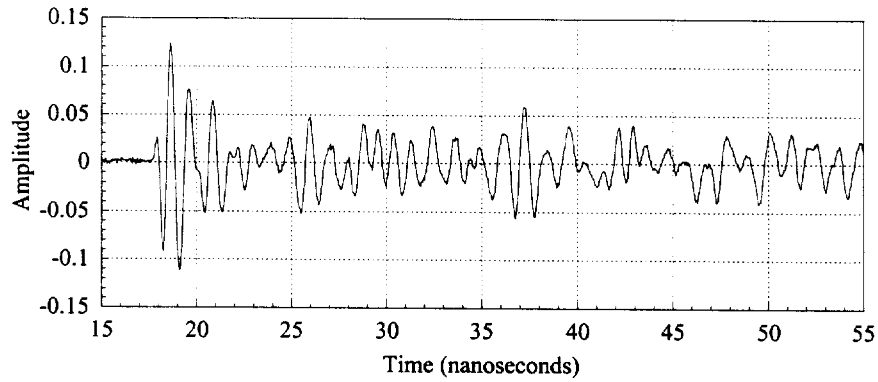

Figure 1-3: Measured signal at sensor (1,7) for a high SNR case.

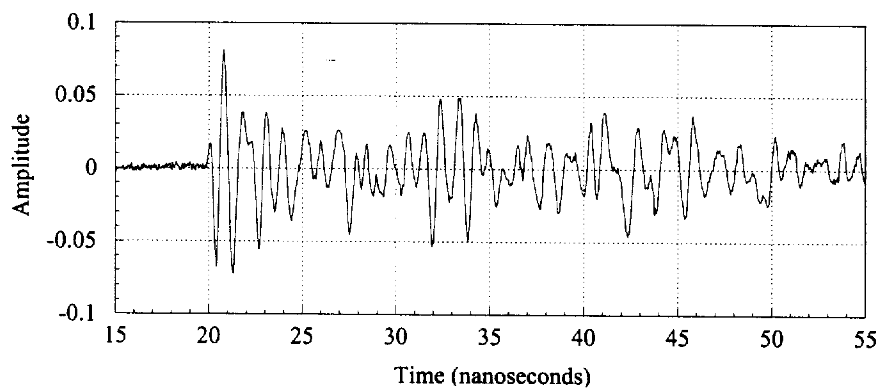

Figure 1-4: Measured signal at sensor (4,4) for a high SNR case.

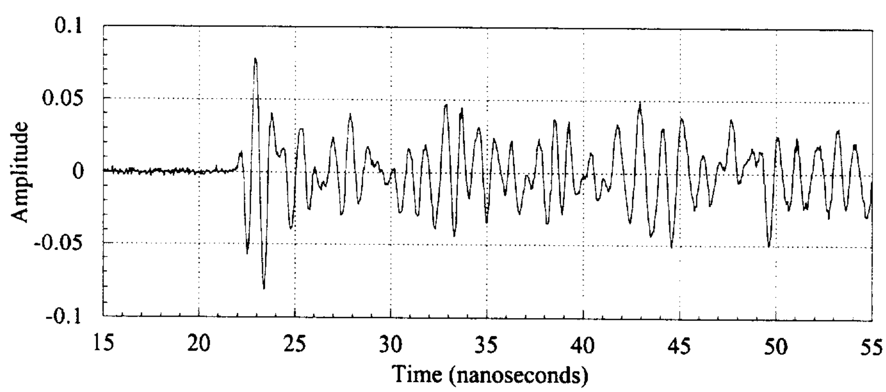

Figure 1-5: Measured signal at sensor (7,1) for a high SNR case.

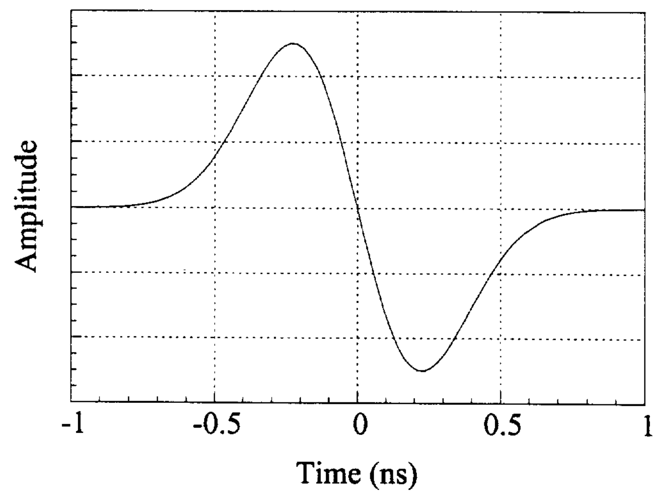

Figure 1-6: Transmitted pulse shape

$$p_1(t) = A_1(t - t_d)\exp\left[-2\pi\left(\frac{t-t_d}{\tau_m}\right)^2\right]. \tag{1.2}$$

This equation is plotted in Figure 1-6 for a hypothesized impulse width parameter of τ_m=0.8 nanoseconds. This value for τ_m was determined as a best fit to the direct path signal in the measured data.

The response of the receive antenna to this pulse is modeled by the time-derivative of equation 1.2, given as

$$p_2(t) = A_2\left[1 - 4\pi\left(\frac{t-t_d}{\tau_m}\right)^2\right]\exp\left[-2\pi\left(\frac{t-t_d}{\tau_m}\right)^2\right] \tag{1.3}$$

and shown in Figure 1-7, where the parameters have the same interpretation as above. Note the tendency of the antennas to radiate a signal proportional to the derivative of the driving current. This is a general characteristic of antennas [56], but is not a concern in the narrowband case, as the properties of the derivative are well approximated by a phase shift. The implications are that antenna design for UWB systems is a distinct problem from antenna design for more narrowband systems.

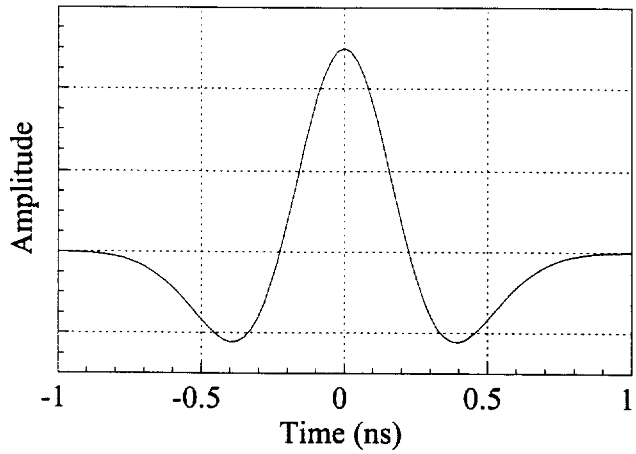

Figure 1-7: Pulse shape at input to demodulator

Taking the Fourier transform of these pulses, the magnitude of the frequency spectra are given by

$$P_1(f) = \frac{A_1 f \tau_m^3}{2\sqrt{2}} \exp\left(-\frac{\pi f^2 \tau_m^2}{2}\right), \tag{1.4}$$

$$P_2(f) = \frac{A_2 \pi f^2 \tau_m^3}{\sqrt{2}} \exp\left(-\frac{\pi f^2 \tau_m^2}{2}\right). \tag{1.5}$$

These equations are plotted in Figure 1-8 and Figure 1-9 using the same impulse width parameter of τ_m=0.8 ns. The bandwidth of these signals is noted. These transforms can be taken utilizing properties of Hermite functions, by representing the transmitted signal as a linear combination of Hermite functions [62],

$$p_n(t) = \sum_k a_k H_k. \tag{1.6}$$

The transform is then given as,

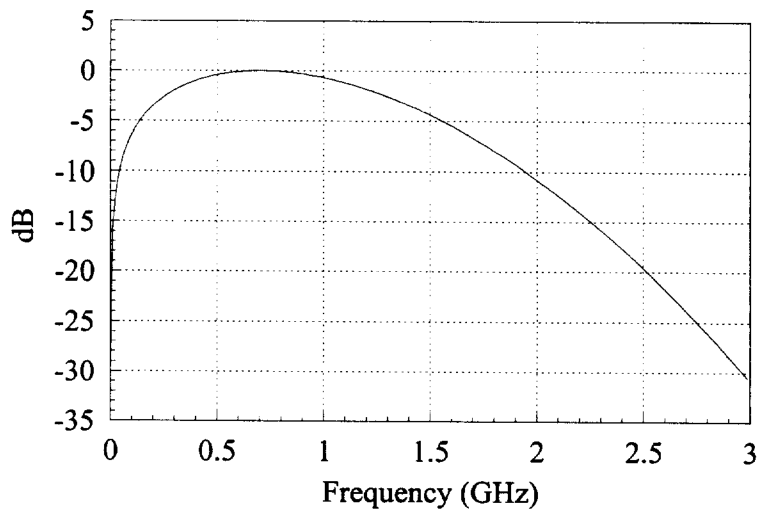

Figure 1-8: Magnitude spectrum of transmitted pulse

$$P_n(\omega) = \sqrt{2\pi} \sum_k (-1)^k a_k H_k(\omega) . \tag{1.7}$$

This representation will be developed further in Appendix A.

The received signal model associated with this waveform is complicated by the fact that transmitted pulses undergo significant shaping in the radiation and propagation processes [56]. In addition, the channel adds multipath components and noise, as seen in Figure 1-3, 1-4 and 1-5. The cumulative effect can result in a received signal which is no longer well modeled by these Gaussian pulses. As discussed in Appendix A, this phenomenon eliminated these sorts of models from having any significant application in this work.

1.4 Overview of the Dissertation

Following the introduction to UWB signals and the motivation for considering them, given in this chapter, Chapter 2 develops the concept of UWB beamforming. In Chapter 3, the properties of UWB arrays are presented, as distinct from those of more narrowband arrays. The unique problems associated with processing UWB signals are also included in the discussion.

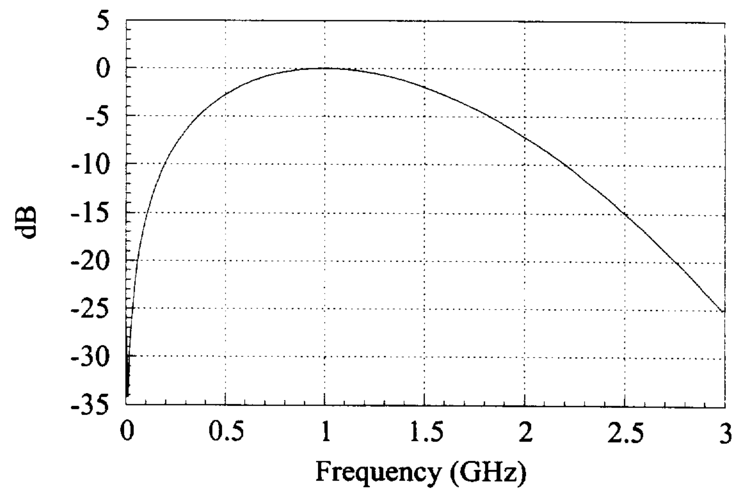

Figure 1-9: Magnitude spectrum at the output of the receive antenna

An iterative solution to the problem of UWB signal detection and identification is introduced in Chapter 4. This algorithm is developed and verified and the post-processing of the results is addressed in both Chapter 4 and Chapter 5. Finally, the processing algorithms are applied to the measured data to recover estimates of the incident signal parameters. This recovered signal information is used in Chapter 6 and Chapter 7 to derive the UWB channel models that form the main result of this work. Chapter 8 concludes.

During the course of this work, a number of techniques are introduced and developed for processing the received UWB signals. A diagram of the various techniques and algorithms introduced or utilized in this work are shown in Figure 1-10. As mentioned, Chapter 2 and Chapter 3 deal with UWB beamforming, in the context of a delay-and-sum beamformer. In Chapter 4, iterative techniques for processing the signals at the output of the delay-and-sum beamformer are introduced, first as the CLEAN algorithm. Modifications which permit the iteration to update the original sensor data, rather then the beamformer output, are made to the CLEAN algorithm, which is then re-named the Sensor-CLEAN algorithm. The output of the Sensor-CLEAN algorithm may contain artifacts due to noise or multiple detections of the same signal. Also in Chapter 4, a technique called the Wave-Map algorithm is developed to post-process the output of the Sensor-CLEAN algorithm with a goal of combining multiple detections which likely belong to the same incident signal. In Chapter 5, a technique called the Arrival Combiner is introduced, which combines the outputs of multiple Wave-Maps, run at different resolutions, to reduce the probability of false signal detections. The output of the Arrival Combiner consists of a list of the time and angle-of-arrival of the detected signals, as well as the recovered waveforms. This is the information that is used to characterize the UWB channel.

Delay-and-sum beamforming is a well known operation, as is the CLEAN algorithm. The Sensor-CLEAN algorithm, the Wave-Map algorithm and the Arrival Combiner, however, are all introduced and developed in this work, to deal with problems inherent in the processing of UWB signals.

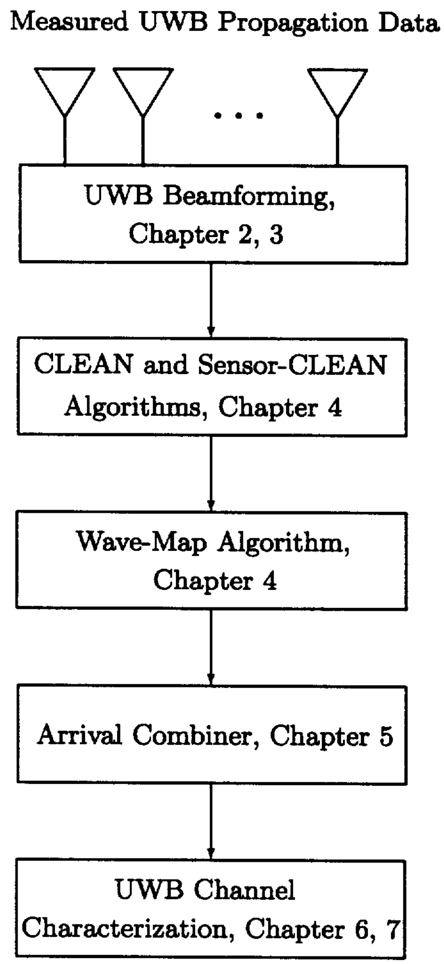

Figure 1-10: Hierarchy of the algorithms developed in this work for processing the UWB signals.

Chapter 2

Ultra-Wideband Array Signal Processing

2.1 Narrowband vs. Ultra-Wideband Array Signal Processing

Fundamental differences exist between the classical array signal processing techniques, predicated on the incidence of narrow-band signals, and the problem of interest here, where the signals have significant fractional bandwidth. In the narrowband case, the signal is generally assumed to be present at all sensors during the observation interval, and to maintain a constant envelope during this time. These assumptions lead to the concept of the array factor as a time-invariant measure of the beamformer response to an incident signal from a particular direction. The beamformer then imparts only a scaling in amplitude as a function of the look direction, but does not affect the time variation of the incident signals. A body of literature has been developed to handle problems such as source location and sidelobe reduction for the narrowband case [16], [20], [23], [32].

Given the impulsive nature of the UWB signals considered in this work, the assumption of a constant envelope does not hold. In fact, the signal is not even guaranteed to be present at all sensors at the same instant in time. Further, UWB signals are not well approximated by a tone, and therefore a time-shift is not well approximated by a phase-shift. These differences eliminate many of the established narrowband techniques for processing signals at the output of an array of sensors from direct application to this problem.

For the case of wideband signals, a general approach to determining directional information involves either breaking the problem down into a collection of narrowband problems via filtering, channelization or the use of a delay-and-sum beamformer [4], [16]. In the channelized solutions, an aperture taper might then be applied to each channel in order to achieve sidelobe suppression. A solution such as this is generally accomplished at the expense of time-resolution and is therefore not well-suited to the application at hand.

Other direct techniques for angle-of-arrival (AOA) determination from array data, such as constrained optimizations, require relatively strong assumptions on the form of the incident signals. The performance of these techniques tends to degrade rapidly in the presence of variations from the assumed signaling functions. Again, the time varying nature of the received UWB signals, seen earlier in Figure 1-3, Figure 1-4, and Figure 1-5, precludes the use of these sorts of techniques, since it is difficult to predict the precise shape of the received signals, and therefore the contribution of individual signals to the constraint equations.

As mentioned above, the incident UWB signals are not well modeled as identical to within a phase-shift at all sensors, and the assumption that the signal maintains a constant envelope during interaction with the sensors in the array does not hold in the UWB case. As a consequence, the Fourier analogy between the aperture and the antenna pattern, as exists in the narrowband case, does not hold for UWB beamforming. This then eliminates the concept of aperture tapers for sidelobe reduction. Instead, considering Figure 2-1, in the case of a delay-and-sum beamformer, the maximum achievable peak-to-sidelobe level ratio over all angles-of-arrivals for a linear array of M elements with sensors weights $\{a_m\}_{m=0}^{M-1}$ upon incidence of UWB signals is

$$\begin{aligned} PSL &= \frac{\sum\limits_{m=0}^{M-1} a_m}{\max\{a_m\}_{m=0}^{M-1}} \\ &\leq M, \end{aligned} \tag{2.1}$$

where this expression assumes that the incident pulses do not interfere in the sidelobe region. This relation can be seen as follows. First assume a constraint exists on the sensor weights such that $\sum_{m=0}^{M-1} a_m = 1$. Then suppose that a set of sensor weights exists which provides a peak-to-sidelobe ratio of better than M. Then either $\max\{a_m\}_{m=0}^{M-1} < 1/M$, in which case

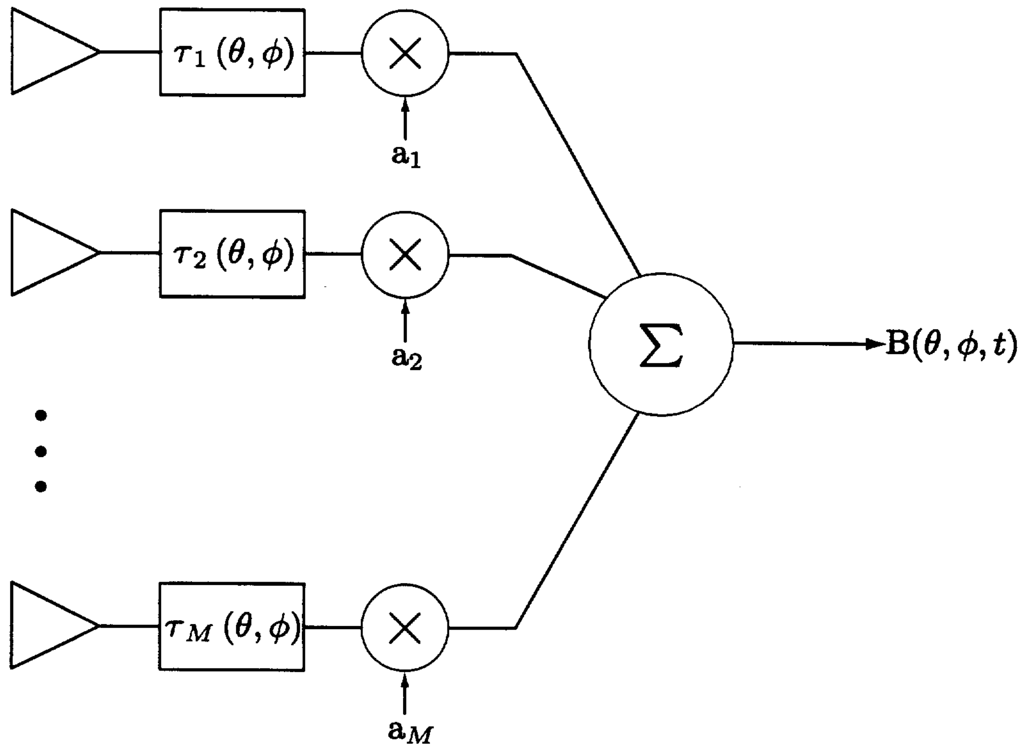

Figure 2-1: A delay-and-sum beamformer, with the steering delay for sensor n specified by $\tau_n(\theta,\phi)$ and the weight by a_n.

the constraint cannot be met, or $\sum_{m=0}^{M-1} a_m > 1$, which again violates the constraint. Thus uniform weighting of the aperture provides the best achievable peak-to-maximum sidelobe level for UWB beamforming. This expression also holds in the case of higher dimensional arrays and plane wave incidence, with the generalization that M corresponds to the ratio of the total number of elements in the array to the number which lie on any line segment drawn through the array. Note that if signal level fluctuations exist from sensor to sensor, the inequality (2.1) will be strict.

Implicit in the limit on the achievable peak-to-sidelobe level in equation (2.1) is a limit on the dynamic range available at the output of the UWB beamformer. It is possible then, that UWB beamforming alone is not capable of resolving the incident signals with sufficient dynamic range to adequately characterize the UWB communication channel. In other words, under the assumption that signals arriving with an amplitude of less than that of the largest sidelobe cannot be reliably identified, a technique for increasing the dynamic range of the UWB beamformer output is needed. Note that for the work presented here, the angular resolution of the array is accepted and no discussion is undertaken on increasing it beyond the physical limit established by the array.

A goal of this research is therefore to develop an appropriate processing technique for resolving the incident UWB signals over a large enough dynamic range to adequately characterize the UWB propagation channel. Given the fractional bandwidth of the baseband UWB signals considered here, it is of interest to investigate time-domain solutions to the problem, as well as methods that do not exhibit a strong dependence on the shape of the received signal. This chapter develops the properties of the UWB beamformers which comprise the first stage in the processing of the incident signals.

2.2 UWB Delay-and-Sum Beamforming

Given the fractional bandwidth of the UWB signals and the corresponding lack of a time-invariant Fourier analogy between the aperture and the array pattern, a uniformly-shaded, delay-and-sum beamformer is applied to the data. In order to implement this beamformer, the delay equations describing propagation of the signal across the array are needed. Consider the delay-and-sum beamformer in Figure 2-1, with a regularly-spaced, linear array of sensors and $a_n = a_m$, for all m, n. Then, as in Figure 2-2, with a plane wave incident at an azimuth angle of θ degrees with respect to broadside, the relative propagation distance between any two sensors is $\mathrm{d}\sin\theta$. In order to resolve both the azimuth angle-of-incidence and the elevation angle, in one hemisphere, another dimension must be added to the array. This leads to the planar structure shown in Figure 2-3. In this case, the incremental delay in the x-direction is given by $(d_x/c)\cos\theta\sin\phi$ and in the y-direction by $(d_y/c)\sin\theta\sin\phi$ where d_x is the sensor spacing in the x-direction, d_y is the sensor spacing in the y-direction and ϕ is the elevation angle-of-arrival.

In theory, the delay-and-sum beamformer of Figure 2-1 can be analyzed in either the time or frequency domain. In the frequency domain, its response can be described at a single frequency by the narrowband array factor, and temporally the array can be described by the impulse

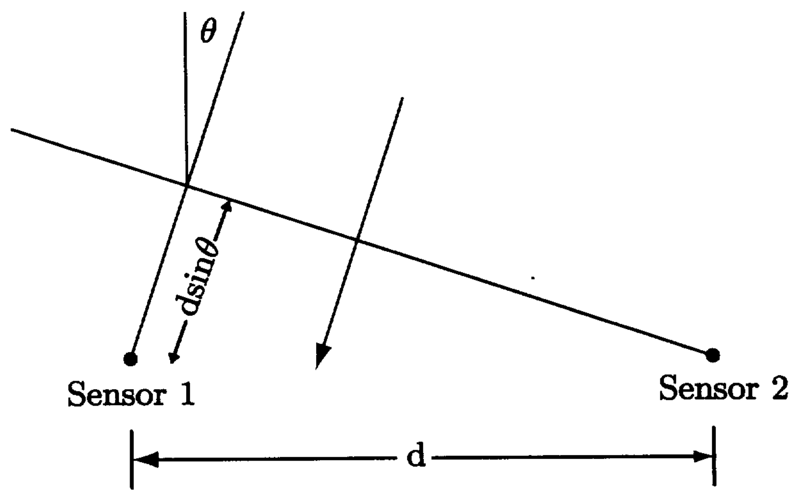

Figure 2-2: Differential propagation distance between sensors for plane wave incidence.

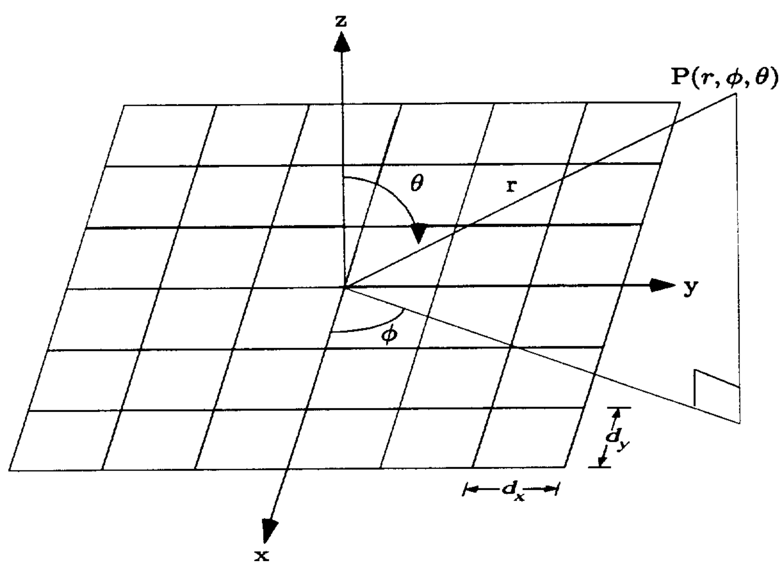

Figure 2-3: Planar array geometry and definitions

response. For the general case of a planar array, the array factor at a single frequency is given as [3]

$$AF(k, \phi, \theta) = \frac{\sin\left(\frac{M}{2}\psi_{\mathrm{x}}\right)}{\sin\left(\frac{1}{2}\psi_{\mathrm{x}}\right)} \times \frac{\sin\left(\frac{N}{2}\psi_{\mathrm{y}}\right)}{\sin\left(\frac{1}{2}\psi_{\mathrm{y}}\right)}, \tag{2.2}$$

where

$$\psi_x = kd_{\mathrm{x}}\left(\cos\theta_{\mathrm{o}}\sin\phi_{\mathrm{o}} - \cos\theta\sin\phi\right) \tag{2.3}$$

and

$$\psi_y = kd_{\mathrm{y}}\left(\sin\theta_{\mathrm{o}}\sin\phi_{\mathrm{o}} - \sin\theta\sin\phi\right) \tag{2.4}$$

for $k = \frac{2\pi}{\lambda}$ radians/meter. Here θ_{o} represents the azimuth angle of incidence, while θ represents the beamformer azimuth look direction. The elevation angle of incidence is given by ϕ_{o} and the beamformer elevation look direction is denoted by ϕ. In addition, N is the number of sensors per row of the array, M is the number of sensors per column of the array, d_x is the sensor spacing in the x-direction and d_y is the sensor spacing in the y-direction.

As mentioned, given the fractional bandwidth of the signals involved here, it is preferable to work in the time-domain. For a time-domain description of the array, consider the impulse response. Assuming isotropic sensors, the impulse response for a planar array, with uniform spacing in the x and the y-directions, is derived from the delay-and-sum operations as

$$h(t) = \sum_{n=0}^{N}\sum_{m=0}^{M}\delta\left(t - n\alpha - m\beta\right), \tag{2.5}$$

where

$$\alpha = \frac{d_{\mathrm{x}}}{c}\left(\cos\theta_{\mathrm{o}}\sin\phi_{\mathrm{o}} - \cos\theta\sin\phi\right), \tag{2.6}$$

$$\beta = \frac{d_{\mathrm{y}}}{c}\left(\sin\theta_{\mathrm{o}}\sin\phi_{\mathrm{o}} - \sin\theta\sin\phi\right) \tag{2.7}$$

and the angles have the same interpretation as above.

In the event that the incident radiation is due to a near field source, the wavefront will display curvature, which implies that the previous results for time-of-arrival of a far-field source are not applicable. The radial distance to the source is measured from the center of the array, and the distance to the sensor of interest is measured relative to the array center. In this case, the differential distance between propagation to the center of the array and propagation to the sensor located at (nd_x, md_y) meters away is given by

$$\Delta r_{mn} = r - \sqrt{r^2 - 2r\sin\theta\left(nd_x\cos\varphi + md_y\sin\varphi\right) + \left(md_x\right)^2 + \left(nd_y\right)^2} \tag{2.8}$$

The associated propagation delay to sensor (n, m) is then given by $\Delta r_{mn}/c$. It will be assumed in this work that all signals are incident with planar wavefronts. No attempt will be made to optimize the processing for non-planar wavefronts.

For the forty-nine element planar array utilized in the measured UWB data described in Chapter 1, the array factor at a single spatial frequency takes the form

$$\begin{aligned} A\left(k_o, \theta, \theta_o\right) &= \frac{\sin\left(\frac{7}{2}k_{\mathrm{o}}d_x\left(\sin\theta\sin\phi - \sin\theta_{\mathrm{o}}\sin\phi_{\mathrm{o}}\right)\right)\sin\left(\frac{7}{2}k_{\mathrm{o}}d_y\left(\cos\theta\sin\phi - \cos\theta_{\mathrm{o}}\sin\phi_{\mathrm{o}}\right)\right)}{\sin\left(\frac{1}{2}k_{o}d_x\left(\sin\theta\sin\phi - \sin\theta_{o}\sin\phi_{\mathrm{o}}\right)\right)\sin\left(\frac{1}{2}k_{o}d_y\left(\cos\theta\sin\phi - \cos\theta_{\mathrm{o}}\sin\phi_{\mathrm{o}}\right)\right)} \\ &= A_x\left(k_{\mathrm{o}}, \theta, \theta_{\mathrm{o}}, \phi, \phi_{\mathrm{o}}\right)A_y\left(k_{\mathrm{o}}, \theta, \theta_{\mathrm{o}}, \phi, \phi_{\mathrm{o}}\right) \end{aligned} \tag{2.9}$$

where $k_{\mathrm{o}} = \frac{2\pi}{\lambda_o}$, as before, θ is the beamformer azimuth look direction, θ_{o} is the azimuth angle-of-incidence, ϕ is the beamformer elevation look direction and ϕ_{o} is the elevation angle-of-incidence. This illustrates the principle of pattern multiplication, which holds for the array factor at a single frequency.

This array can also be interpreted in the time domain by the convolutional model, using the appropriate set of delta functions to represent the relative delays at which the signals from the various sensors are summed to form the beampattern, according to,

$$h\left(t, \varphi, \varphi_o\right) = \sum_{n=0}^{3} \sum_{m=0}^{3} \delta\left(t \pm 2nx \pm 2my\right), \tag{2.10}$$

where

$$x = \frac{1}{2}\frac{d_y}{c}\left(\cos\theta \sin\phi - \cos\theta_o \sin\phi_o\right) \tag{2.11}$$

and

$$y = \frac{1}{2}\frac{d_x}{c}\left(\sin\theta \sin\phi - \sin\theta_o \sin\phi_o\right). \tag{2.12}$$

This time domain approach is a more useful characterization for UWB beamforming. Note that both the frequency domain and the domain representations make the assumption that all sensors contribute, in other words no sensor is shadowed from the signal.

Since the Fourier transform relation between the aperture and the pattern does not hold for the incidence of UWB signals upon the array, consider a general equation for the uniformly-shaded, delay-and-sum beamformer output as the form most applicable to UWB waveform processing,

$$B\left(\theta, \phi, t\right) = \sum_{n} s\left(t + t_n\left(\theta_o, \phi_o\right) - \tau_n\left(\theta, \phi\right)\right), \tag{2.13}$$

where the delay at sensor n, $\tau_n(\theta, \phi)$, is explicitly a function of the beamformer azimuth and elevation look direction.

Evaluating this equation for the case of a uniformly-shaded linear array of M elements and a signal incident at time $t = 0$ gives

$$B(\theta, t) = \frac{1}{2\pi} \int_{-\infty}^{\infty} S(\omega) \frac{\sin\left(M \frac{\omega}{2} \frac{d}{c} \gamma\right)}{\sin\left(\frac{\omega}{2} \frac{d}{c} \gamma\right)} e^{j\omega t} d\omega,$$

where

$$\gamma = \sin\theta_{\mathrm{o}} - \sin\theta,$$

and for an $M \times M$ planar array, the equation becomes

$$B(\theta, \phi, t) = \frac{1}{2\pi} \int_{-\infty}^{\infty} S(\omega) \frac{\sin\left(M \frac{\omega}{2} \frac{d}{c} \gamma_x\right)}{\sin\left(\frac{\omega}{2} \frac{d}{c} \gamma_x\right)} \frac{\sin\left(M \frac{\omega}{2} \frac{d}{c} \gamma_y\right)}{\sin\left(\frac{\omega}{2} \frac{d}{c} \gamma_y\right)} e^{j\omega t} d\omega,$$

where

$$\gamma_{\mathrm{x}} = \sin\theta_{\mathrm{o}} \sin\phi_{\mathrm{o}} - \sin\theta \sin\phi$$

and

$$\gamma_{\mathrm{y}} = \cos\theta_{\mathrm{o}} \sin\phi_{\mathrm{o}} - \cos\theta \sin\phi$$

Again, the principle of pattern multiplication for UWB arrays is seen to hold in the integrand, at a single frequency. This implies that the array response at any angle is the superposition of the array response to each frequency component, at the current look direction.

Equation (??) also defines the existence of the beamformer pattern sidelobes as a function of frequency. In order to reduce the sidelobes in the beamformer pattern, the kernel

$$\frac{\sin\left(N \frac{\omega}{2} \frac{d}{c} \gamma\right)}{\sin\left(\frac{\omega}{2} \frac{d}{c} \gamma\right)} \tag{2.14}$$

where

$$\gamma = \sin \theta_o - \sin \theta \tag{2.15}$$

must be constrained to be as close to a constant value over the frequencies in the support of $S(\omega)$ as possible, so that the spectrum of $S(\omega)$ is not altered by the beamformer. This implies that for a fixed intersensor distance d, a larger value of N will allow for a larger peak-to-sidelobe level. This is in accordance with the time-domain analysis, from which the peak-to-sidelobe level is limited to the number of elements in any linear configuration.

Having established some of the fundamental differences between UWB and narrowband arrays, it is now appropriate to study the properties of UWB arrays in greater detail. This is the subject of the next chapter.

Chapter 3

Properties of Ultra-Wideband Arrays

3.1 Characterization of the Time-Domain Beamformer Response

Following as in equation (2.13), let the output of a uniformly-shaded delay-and-sum beamformer for a linear array of sensors, steered to an azimuth look direction of θ radians, on incidence of a plane wave with time variation $s(t)$ from an azimuth angle of θ_o radians, be represented by [56]

$$B(\theta, t) = \sum_n b_n(\theta_o)\, s\left(t - n\frac{d}{c}(\sin\theta_o - \sin\theta)\right). \tag{3.1}$$

where $b_n(\cdot)$ is the antenna pattern associated with an individual element. As before, d represents the inter-element spacing and c is the speed of light. This equation assumes that the same signal is received by all elements of the array. If each sensor in the array has the same antenna pattern, it can be removed from the summation. The expression

$$\sum_n s(t - n\frac{d}{c}(\sin\theta_o - \sin\theta)) \tag{3.2}$$

is then the equivalent array factor for the time-domain case and the signal $s(t)$. Just as the expression for the array factor in the narrowband case was dependent on the assumed sinusoidal signal characteristics, the time-domain expression here also explicitly depends on the received waveform. Neglecting a constant, the array factor of equation 3.2 represents the pattern associated with a uniformly-shaded linear array of isotropic sensors on incidence of a plane wave with time variation $s\,(t)$ from an azimuth angle of θ_o degrees.

Consider an example from [46] to illustrate this time-domain beamforming process. A uniformly-shaded linear array of three sensors is shown in Figure 3-1, with a sensor spacing of $2\lambda_o$. Here, λ_o is defined as the wavelength of a received monocycle, also shown in Figure 3-1. Assume this monocycle is incident upon the array at broadside, so that the signal is received by each sensor at the same instant in time. As shown in 3-2 (a), at broadside the beamformer output is a replica of the incident signal, scaled in amplitude by the number of sensors; the sensor outputs add "coherently". If the beamformer is instead steered so that the delays cause the monocycles to add at $\frac{1}{2}\lambda_o$ out of "phase", corresponding to a look direction of 14.48°, the waveform in Figure 3-2 (b) is output from the beamformer. At a look direction of 30°, the output waveform consists of three consecutive monocycles, shown in Figure 3-2 (c). As the look direction progresses to angles greater than 30°, the monocycle continues to appear in the output, but the spacing between successive signals increases. Thus, at angles less than 30°, the energy in the output waveform varies, but above 30° the energy in the output waveform is constant, but the temporal distribution of the energy varies. In this case, 30° defines the critical angle for the beamformer, θ_c. In general, θ_c is defined for a linear array of sensors as the angle at which $cT = d\sin\theta$, where T is the time duration of the impulse.

This variation in the output pattern as a function of time is in contrast to the narrowband case, where the array pattern is constant as a function of time, and for an N element linear array is given by

$$B\,(\theta) = \frac{\sin\left(\frac{N\pi d}{\lambda}\sin\theta\right)}{\sin\left(\frac{\pi d}{\lambda}\sin\theta\right)}. \tag{3.3}$$

Given that the UWB beamformer output is a function of the incident waveform and that

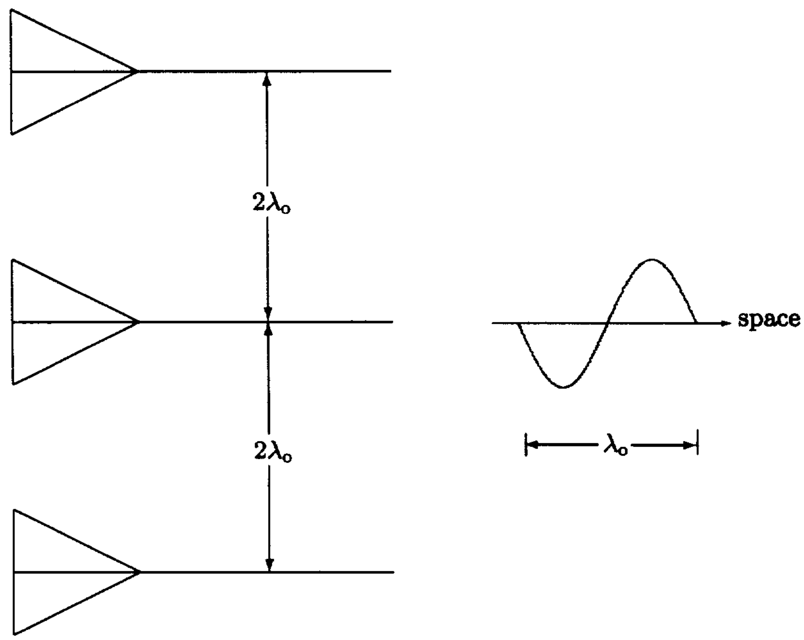

Figure 3-1: Three element UWB receive array and the received monocycle.

the transmitted UWB signals can undergo significant shaping in the radiation and propagation processes, it is impossible to predict the beamformer output patterns that will result when operating on measured data. For the sake of example, the second derivative Gaussian pulse, denoted by $p_2(t)$, will be used here to demonstrate some typical patterns.

Consider first the output of a three element linear array with inter-sensor spacing of $d = 1.0$ meter, on broadside incidence of a plane wave with time variation $p_2(t)$. Figure 3-3 (a) shows the beamformer response to the incident waveform when steered to the angle-of-incidence at broadside. The signal is not distorted by the array and is scaled in amplitude by the number of sensors. Figure 3-3 (b) shows the beamformer output at a look direction of 17°. The waveform has been distorted, and now has peak amplitude equal to that of a single incident impulse. Figure 3-3 (c) shows the beamformer output at 34°, approximately the critical look angle, θ_c, for this array and waveform. The waveforms from each sensor are now distinct and emerge from the beamformer sequentially in time. As the look direction increases beyond θ_c, the distance in time between successive pulses is seen to increase, to a maximum value at a look direction of 90°shown in Figure 3-3 (d). The maximum amplitude of the off-peak waveform establishes the

(a) UWB beamformer output at a look direction of 0°

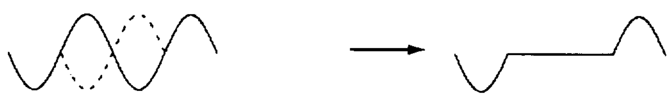

(b) UWB beamformer output at a look direction of 14.48°

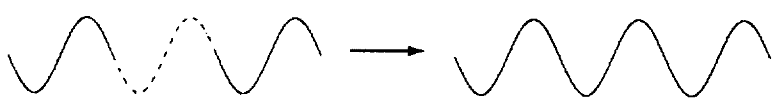

(c) UWB beamformer output at a look direction of 30°

(d) UWB beamformer output at a look direction of 45°

Figure 3-2: Time domain UWB beamformer example for the three element UWB array

sidelobe level for the beamformer, and therefore determines the maximum available dynamic range of the beamformer. In this case the maximum sidelobe level is given by the output of a single sensor.

More generally, the maximum sidelobe level of an UWB array will be determined by the number of impulse signals which can add coherently at an off-peak look direction. It is therefore instructive to give another plot of the beamformer output, where the time dependence has been removed and the maximum amplitude at each look direction for across all time instants is recorded. This is called the maximum projection [41], and is given for this three element array

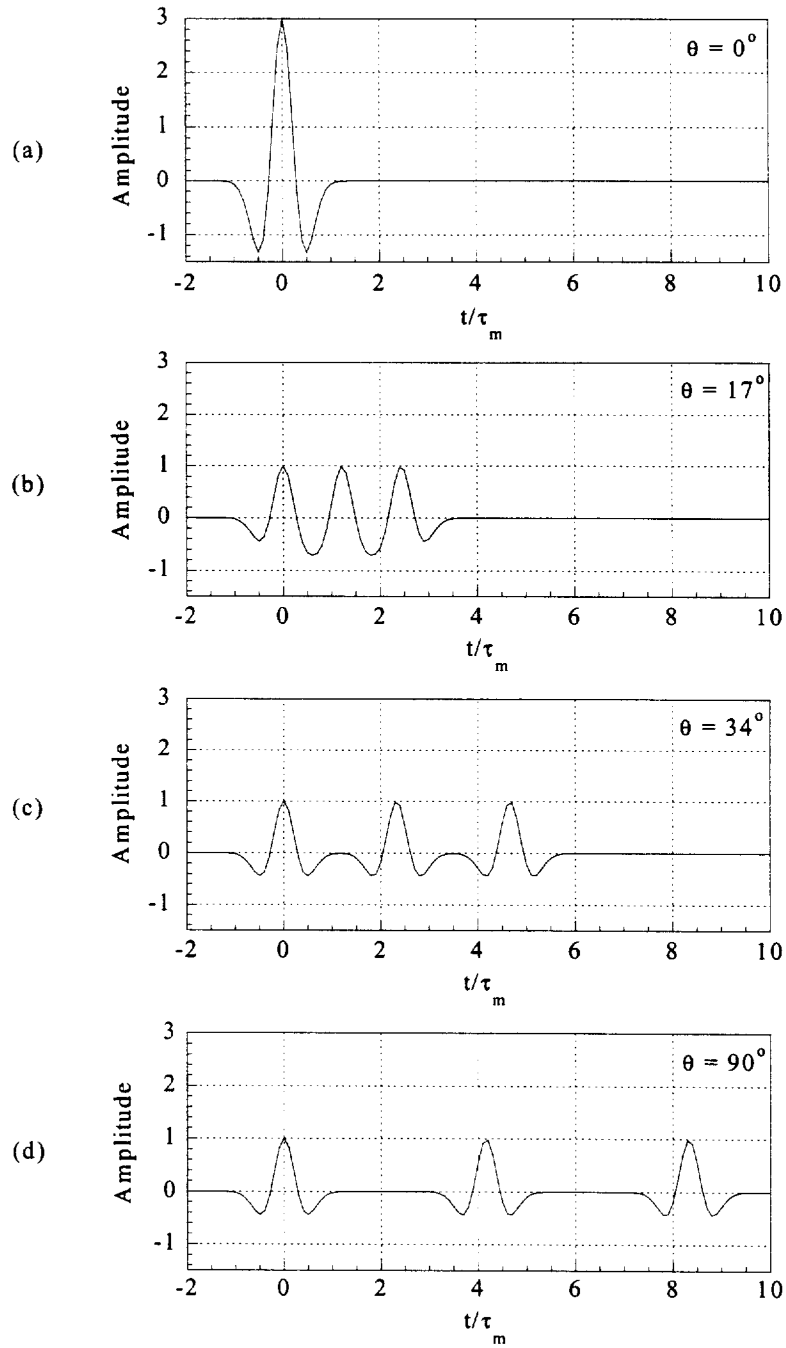

Figure 3-3: Three element beamformer output at the indicated look directions with $d = 1$ meter and $p_2(t)$ incident.

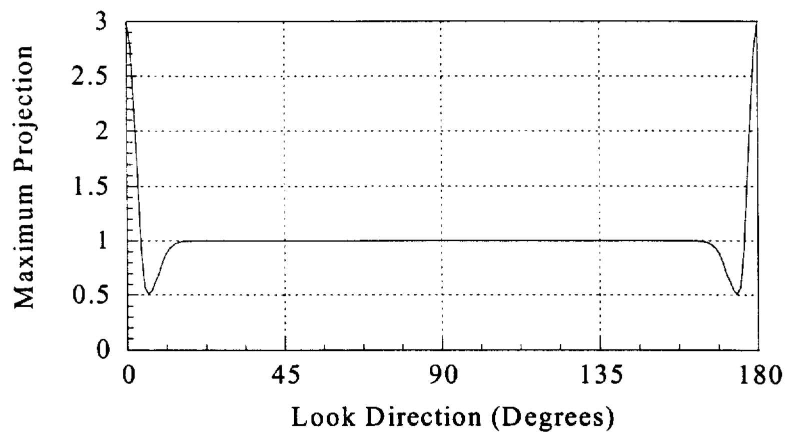

Figure 3-4: Maximum projection of the three element UWB array with $p_2(t)$ incident.

in Figure 3-4. This plot confirms the sidelobe level discussed above. Figure 3-4 also gives some insight into the angular resolution performance of the array, generally taken as proportional to the width of the main lobe.

To emphasize the time dependence of the array pattern, Figure 3-5 gives a plot of the beamformer output versus time and azimuth angle for this array geometry and waveform. Note the location in time and angle of the main response and of the sidelobes.

In order to demonstrate the increasing complexity of the array patterns as the number of elements is increased, Figure 3-6 shows the properties of a seven element linear array, with the same inter-sensor spacing of 1 meter, and 3-7 gives the maximum projection. Of particular note in these plots is the increase in the time extent of the beampattern, and the increase in the peak-to-sidelobe amplitude ratio (PSL) of the beamformer output. The increase in time extent is due to the increase in the propagation distance across the array, and the increase in the PSL is due to the coherent addition of seven sensors to form the on-peak waveform in conjunction with the lack of a mechanism for waveforms to combine coherently at an off-peak look angle.

Proper selection of inter-element spacing is necessary to design UWB arrays for particular scenarios. In fact, just as narrowband arrays might be designed to operate at a particular frequency, perhaps $d = \lambda_o/2$, a UWB array might be designed for a particular pulse width. Consider the narrowband case, where the sensor spacing must be selected so that $d < \lambda/2$, else

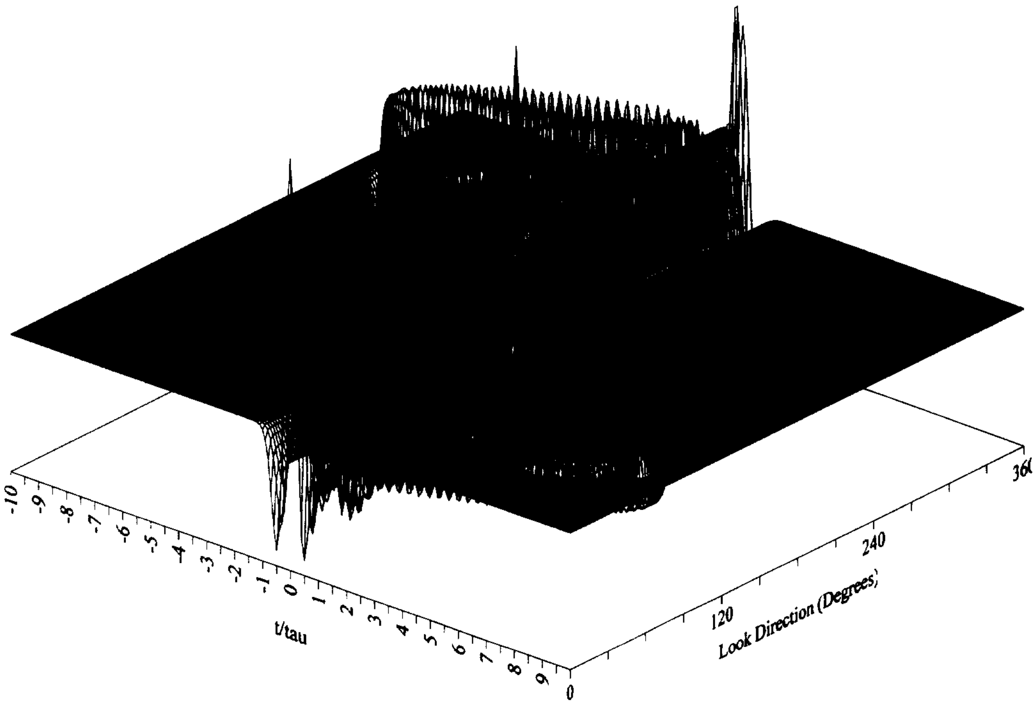

Figure 3-5: Time and angle dependence of the three element array pattern with inter-sensor spacing of 1 meter, upon incidence of $p_2(t)$.

grating lobes form. The trade-off is in overall aperture length L, determined by the number of elements in the linear array multiplied by the inter-element spacing, which determines the angular resolution limit of the array. The same trade exists in UWB arrays, as can be seen in the maximum projection plots for the different values of d, and will be developed formally below. As a prelude to this discussion, Figure 3-8 gives the maximum projection for a seven-element array with inter-element spacing of $d = 0.50$ meters, and Figure 3-9 does the same for $d = 0.152$ meters, the actual spacing used in the planar measurement array. In terms of angular resolution, the difference in the width of the main lobe of the maximum projection in the two plots is noted. Further, for a hypothesized pulse width parameter of $\tau_m = 0.8$ ns, at $d = 0.50$ meters, the critical angle is almost achieved by the array, due to the fact that the pulse length

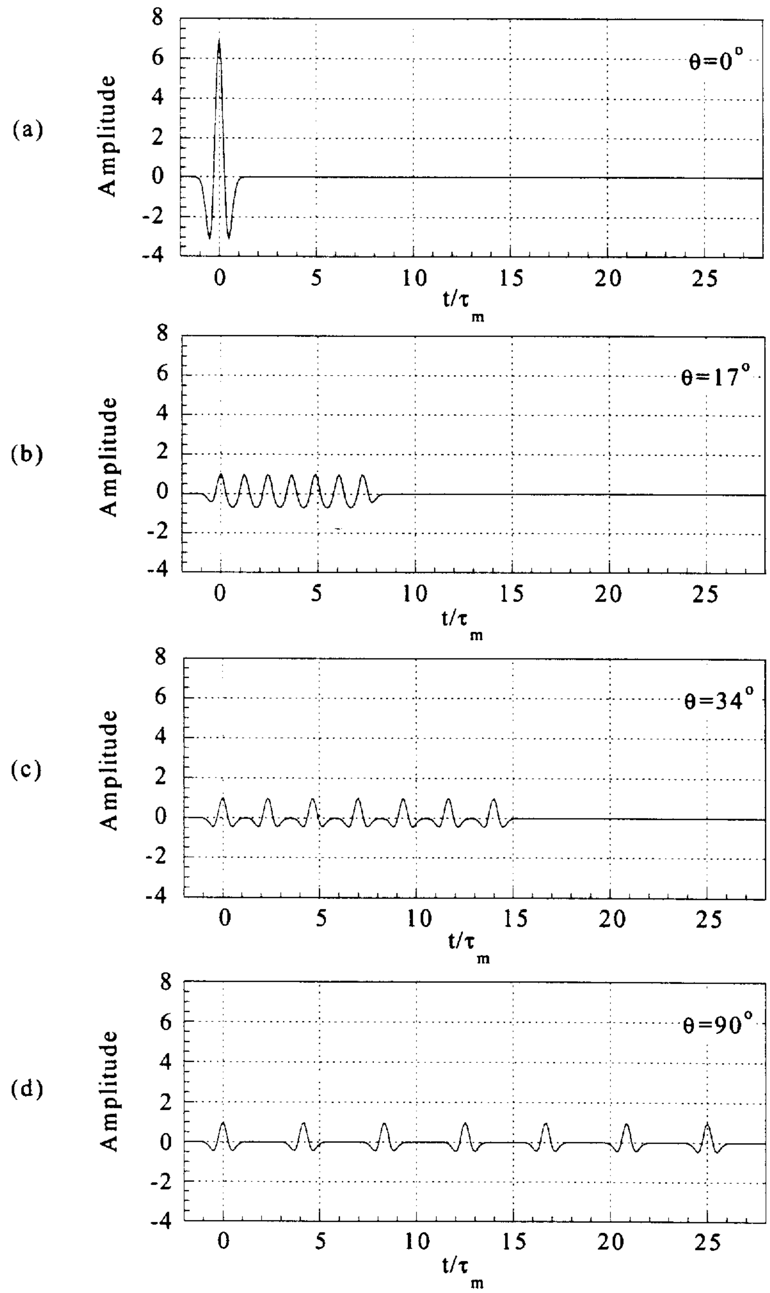

Figure 3-6: Seven element beamformer output at the indicated look directions with $d = 1$ meter and $p_2(t)$ incident.

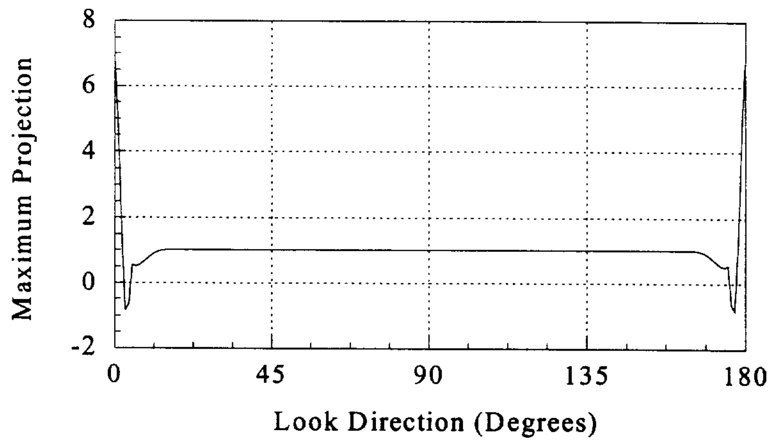

Figure 3-7: Maximum projection for the seven-element linear array with $d = 1$ m

in space is just longer than d. For $d = 0.152$ meters, the critical angle is not achieved.

Increasing the complexity of the array, the patterns associated with the seven by seven element planar array on with which the data was actually measured, shown in Figure 3-10, are given in Figure 3-11 for incidence of a signal with time variation $p_2(t)$ from an azimuth angle of 0°and an elevation angle in the plane of the array. The peak output is now generated by the addition of forty-nine sensors, and the maximum sidelobe is due to the off-peak addition of seven sensors. In order to demonstrate the spatial and temporal extent of these patterns, the response over time and azimuth angle is shown first in Figure 3-12 for an azimuth angle-of-incidence of 45°and an elevation look direction equal to the elevation angle-of-incidence of 90°. In Figure 3-13 the azimuth angle of incidence is 220°and the elevation angle is still 90°. The location in time and angle of the peak response and of the sidelobes can be seen in the plots.

Removing the time dependence from these plots, two examples of the maximum projection for this array are shown in Figure 3-16 and Figure 3-17. Note that even as the number of sidelobes increases, the PSL remains roughly the same as in the seven element linear array, since now up to seven elements can combine at an off-peak look direction.

Next, consider Figure 3-14 and Figure 3-15, where an impulse is incident at an azimuth angle of 180°. The theoretical response of the beamformer versus azimuth and elevation look directions, at the peak response time, is shown for two different elevation angles-of-incidence.

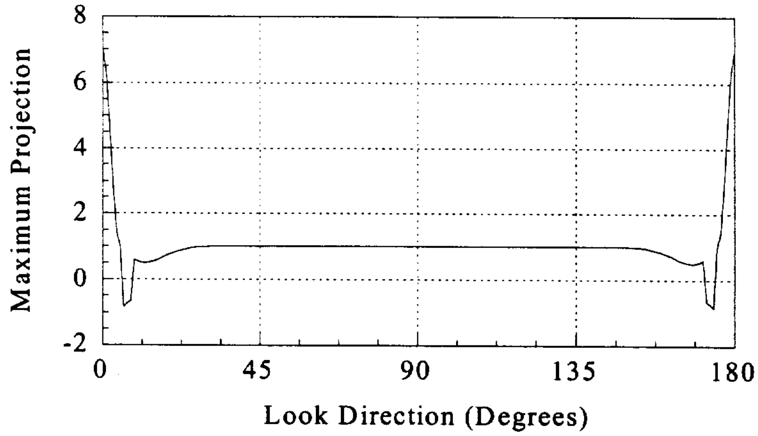

Figure 3-8: Maximum projection for a seven element array with $d = 0.50$ meters and $p_2(t)$ incident from 0°.

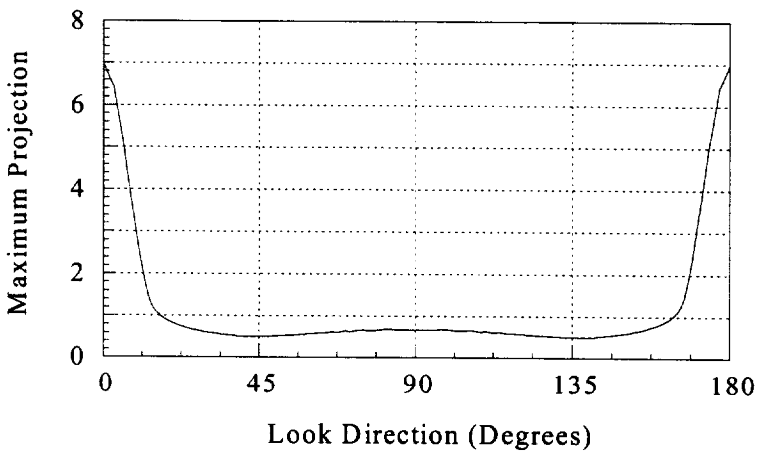

Figure 3-9: Maximum projection for a seven element array with $d = 0.152$ m and $p_2(t)$ incident from 0°.

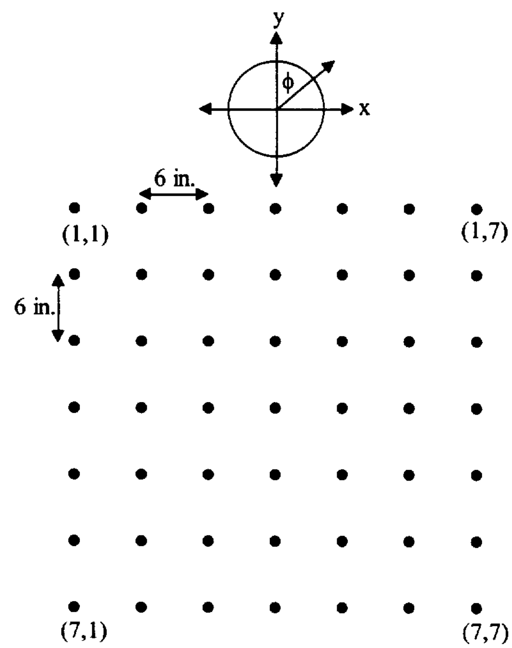

Figure 3-10: Geometry of the array on which measured data was taken.

In the first case, the impulse arrives in the plane of the array, and a response with a single peak is noted. In the second case, with the impulse incident from an elevation angle of 45°, an ambiguity in the response is seen. This is due to the use of a two-dimensional array, which can only resolve elevation angles to within 90°. In other words, the two-dimensional array cannot distinguish whether a signal is incident from above or below the array.

Given the sidelobes inherent in the output of a UWB beamformer, and the lack of a systematic means for controlling them, a technique is needed to increase the dynamic range available at the output of the beamformer, if it is to be used to provide signal information for the characterization of the UWB propagation channel.

3.2 Angular Resolution of UWB Arrays.

The angular resolution performance of an UWB array is defined by the minimum required separation in both azimuth and elevation angles-of-arrival between two signals which are coincident in time, such that the UWB array is able to resolve the signals as distinct. In the narrow-

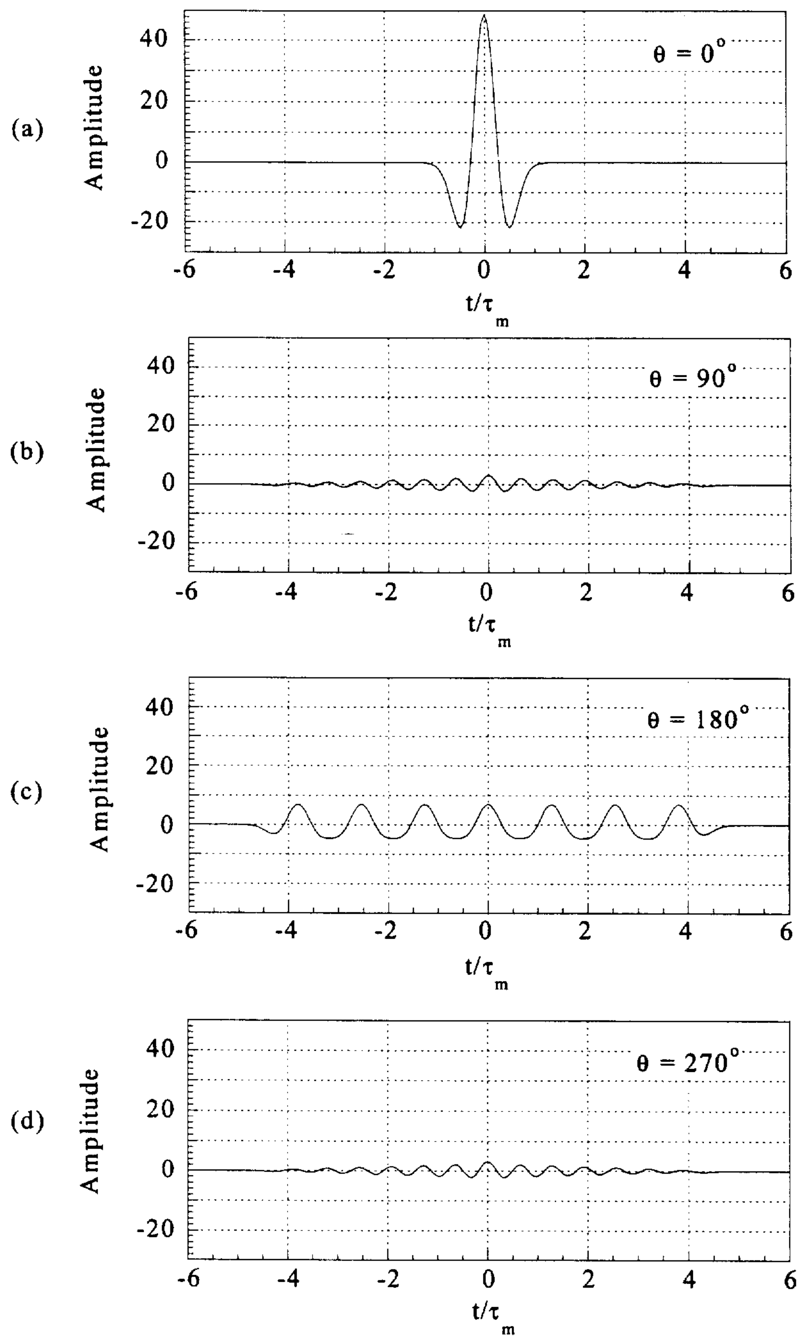

Figure 3-11: Forty-nine element planar array beamformer output on incidence of $p_2(t)$ from 0°, at the indicated look directions.

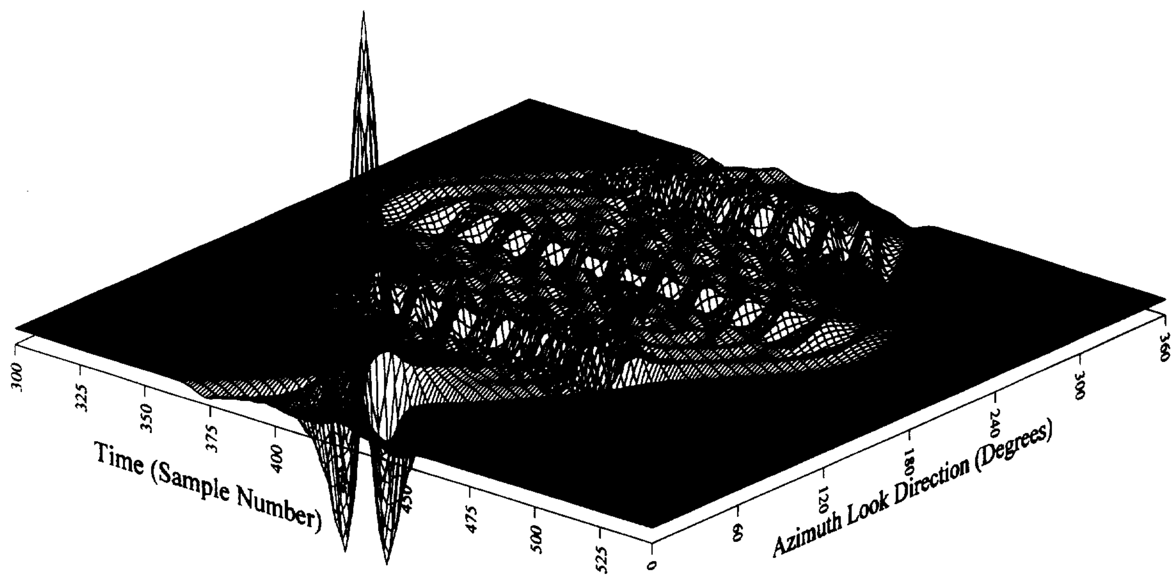

Figure 3-12: 7×7 element planar beamformer response to $p_2(t)$ arriving from an azimuth angle of 45^o and an elevation angle of 90^o.

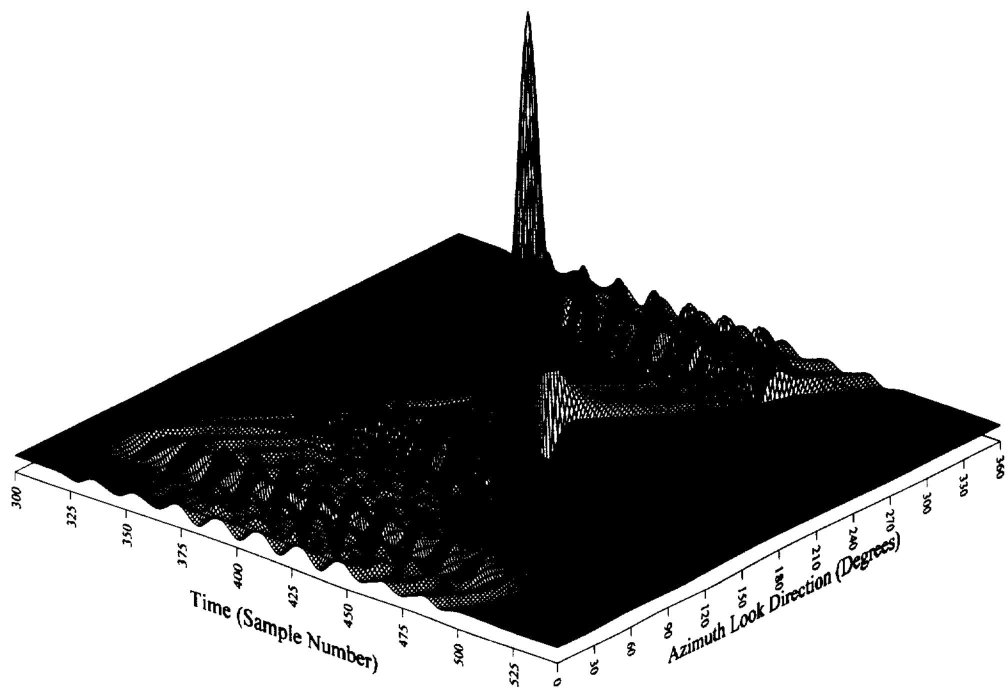

Figure 3-13: Planar beamformer response to $p_2(t)$, incident from an azimuth angle of 220^o and an elevation angle of 90^o.

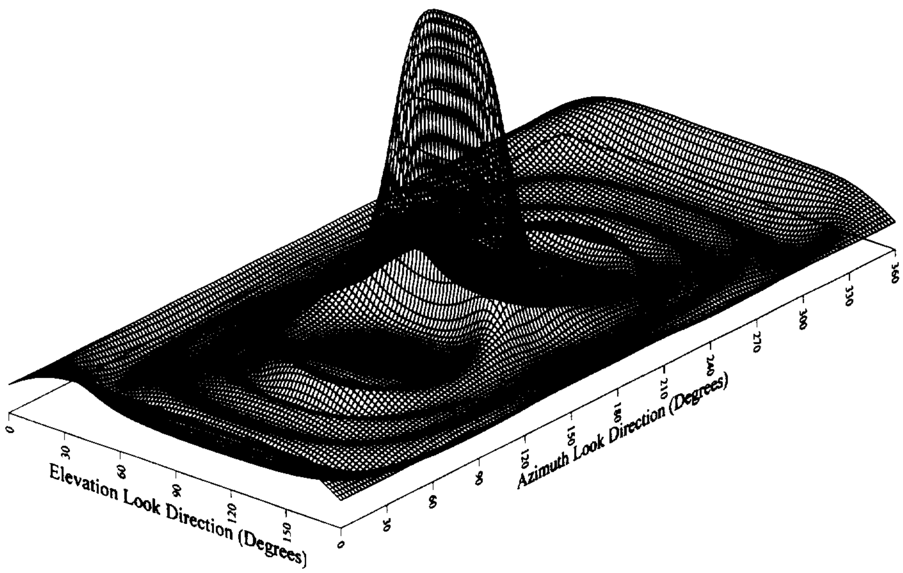

Figure 3-14: Planar beamformer output vs. azimuth and elevation angles at the peak response time, on incidence of $p_2(t)$ from an azimuth angle of 180° and an elevation angle of 90°.

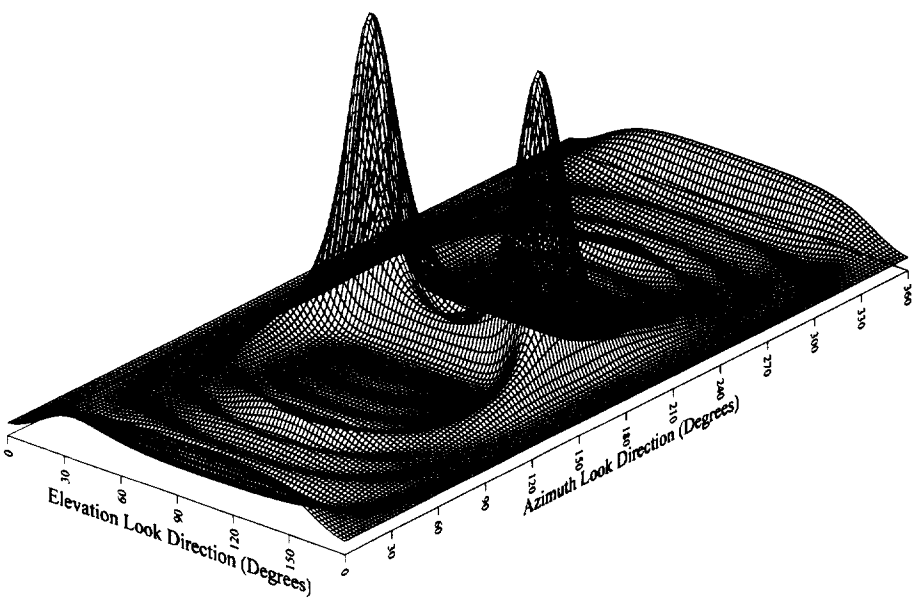

Figure 3-15: Planar beamformer output vs. azimuth and elevation angles at the peak response time, on incidence of $p_2(t)$ from an azimuth angle of 180° and an elevation angle of 45°.

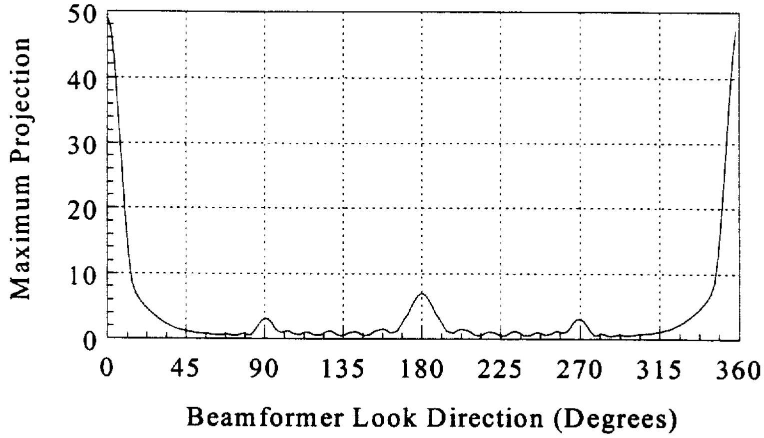

Figure 3-16: Maximum projection for the forty-nine element planar array for incidence of $p_2(t)$ from 0^o.

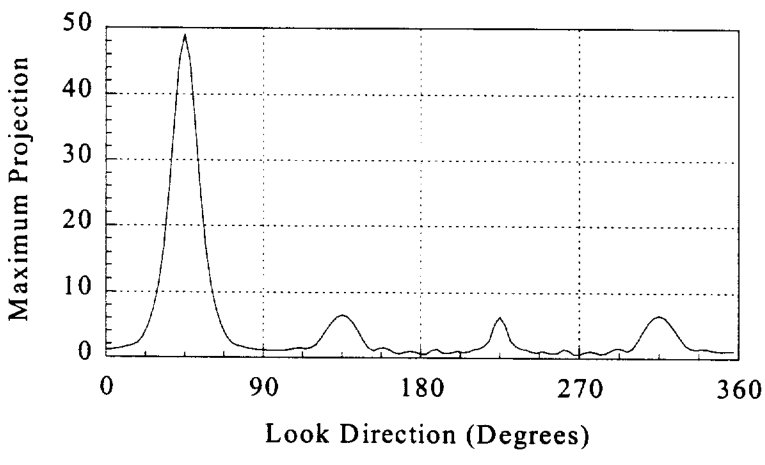

Figure 3-17: Maximum projection for the forty-nine element planar array for incidence of $p_2(t)$ from 45^o.

band case, with the incident signals taken as sinusoids, the angular resolution of a uniformly shaded linear array is typically defined by the Rayleigh resolution limit, given for a large array ($L >> \lambda_o$) as $\lambda_o/Nd = \lambda_o/L$, where λ_o is the wavelength of the incident sinusoid, N is the number of elements in the array, d is the inter-element spacing and L is the length of the array. Hence for a fixed array length, the angular resolution performance of the array is a function of the signal frequency. For the case of an UWB array, the equivalent expression for angular resolution can be given [56] as $ct_p/Nd = ct_p/L$, where c is the speed of light and t_p is the temporal extent of the pulse. This expression holds under the condition that the array is large relative to the spatial extent of the pulse, ct_p. A derivation of this expression is given in [56] assuming that the array is a continuous aperture and a Gaussian pulse is incident. Heuristic justification for this expression is given in Figure 3-18, adapted from [56].

Thus a distinction between narrowband arrays and UWB arrays is in the dependence of the angular resolution on the signal frequency versus the signal duration, respectively. Stated another way, narrowband arrays are often designed to operate at a single frequency, while UWB arrays are designed for a given pulse width.

Note that the in the case of a planar array, the resolution angle will be a function of the angle-of-incidence. For example, using an N element $\times$ N element square array, the array length at broadside is $L = Nd$ meters, while at an incidence angle of 45^o it is $L = Nd\sqrt{2}$ meters.

A plot of the theoretical angular resolution versus the signal bandwidth, where bandwidth is approximated by $1/t_p$, is given in Figure 3-19 for a number of different array lengths. The measured data used in this work was taken on an array with Nd at just under 1 meter.

3.3 Beamformer Response to Measured Data

The beamformer patterns presented in this chapter give some intuition into the performance of UWB arrays. These results correspond to a particular incident signal, however, and as seen in equation (3.2), the pattern is a function of this incident signal and will vary as the incident signal varies. Thus, if the incident waveform is not well known, it is difficult to predict the beampattern that will be generated by the waveform.

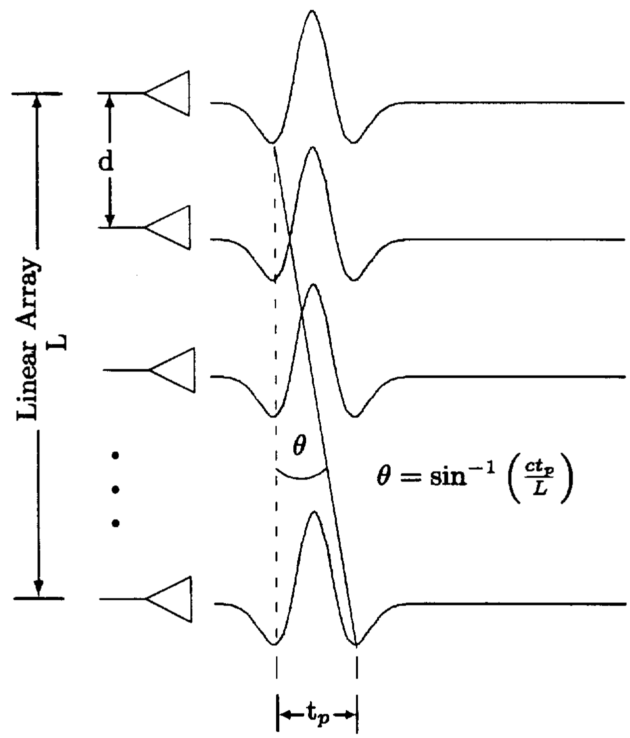

Figure 3-18: Angular resolution capability of a UWB array.

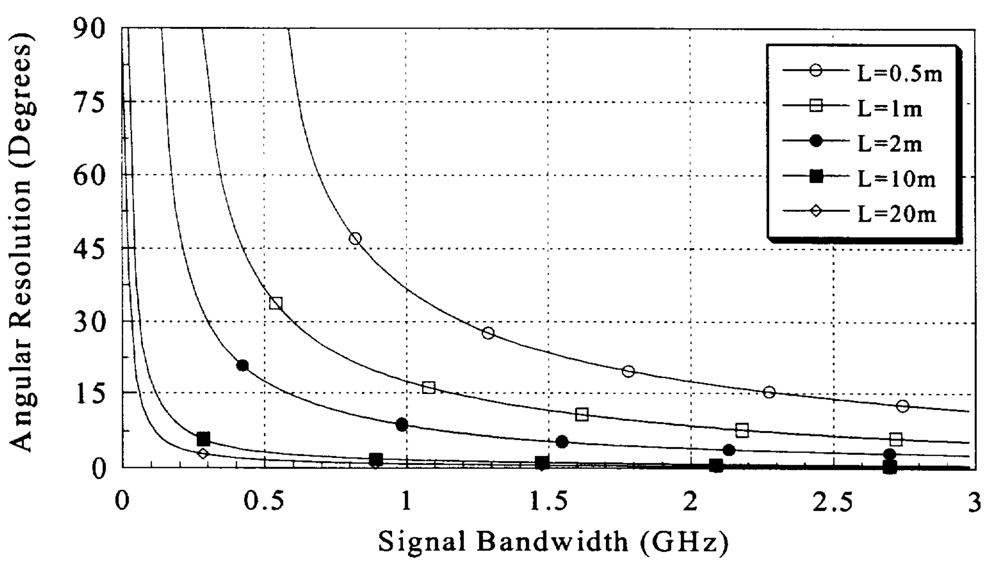

Figure 3-19: Angular resolution versus signal bandwidth.

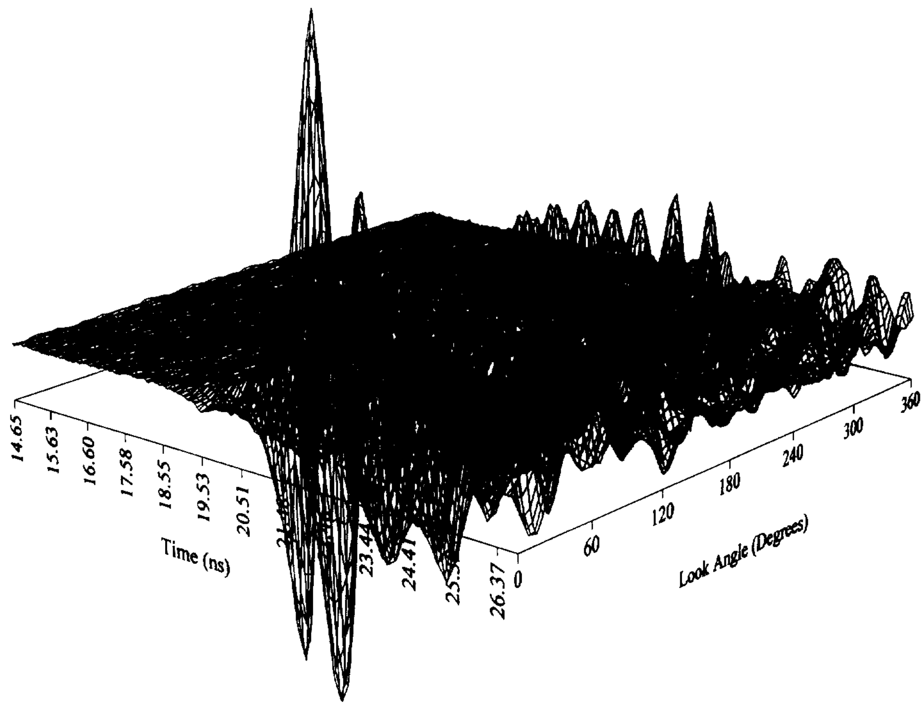

Figure 3-20: Beamformer response to the measured data taken at location P. Elevation look direction is 90^o.

In summary, and to further motivate the problem of sidelobe reduction and signal identification addressed in the next chapter, a plot of the beamformer response to the measured data at location P is shown below in Figure 3-20 over a window in time around the arrival of the direct path signal. In this plot, the direct path signal is easily identified, as are significant additional contributions, due either to sidelobes or multipath. Processing algorithms for UWB sidelobe reduction and signal identification are the subject of the next chapter.

Chapter 4

Iterative Techniques for UWB Array Signal Processing

4.1 Description of the algorithm

Implicit in the limit on the achievable peak-to-sidelobe level in equation (2.1) is a limit on the dynamic range available at the output of the UWB beamformer. It is possible then, that UWB beamforming alone is not capable of resolving the incident signals with sufficient dynamic range to adequately characterize an UWB communication channel. In other words, under the assumption that a signal cannot be reliably identified if it arrives with an amplitude in the beamformer output of less than that of the largest sidelobe, a technique for increasing the dynamic range of the UWB beamformer is needed. As discussed in Chapter 2, the time-variation and the impulsive nature of the received UWB waveforms preclude the use of a direct technique for sidelobe reduction and identification of the incident signals. In the absence of an applicable direct technique, an indirect or iterative solution is attempted.

The technique proposed here for processing the incident UWB signals is based upon the CLEAN algorithm, introduced in [19] for the enhancement of radio astronomical maps of the sky. More generally, the algorithm is related to the Gauss-Seidel relaxation technique [10], a method of successive displacements, and the Gauss-Southwell iteration. The CLEAN algorithm has also found utility in more general antenna sidelobe reduction problems, particularly in the microwave and radar imaging communities [48], [49], [57].

The problem of sidelobe level reduction for UWB arrays can be considered in the context of image restoration. For these problems, techniques have been developed for extracting information from multi-dimensional collections of data. Often, direct inversion to extract source information in these scenarios is not feasible, and a regularized or iterative solution is attempted. One form of iterative solution is given in [27] by the Van-Cittert (or Landweber) equation as

$$\mathbf{t}_{n+1} = \mathbf{t}_n + \gamma\left(\mathbf{g} - \mathbf{D}\mathbf{t}_n\right) \tag{4.1}$$

where $\mathbf{g}$ is a vector representing the image to be restored, formed by concatenating the rows of the image, $\mathbf{t}_n$ represents the restoration result at each iteration and $0<\gamma \leq 1$ is a loop gain term. In this context, $\mathbf{D}$ represents some blurring or distortion function, generally with a circulant structure. The idea is to successively drive the residual term $(\mathbf{g} - \mathbf{D}\mathbf{t}_n)$ to zero, and the iteration is terminated when a norm on this expression is less than some prescribed amount. This iteration converges if all eigenvalues, λ, of $\mathbf{D}$ satisfy $|1 - \gamma\lambda| < 1$ [27].

An iterative restoration algorithm such as equation 4.1 is generally implemented for two reasons. First, in the case of an ill–posed problem, the iteration can be terminated prior to significant noise magnification. Second, the use of this method eliminates the need to directly invert the matrix $\mathbf{D}$ in order to solve the problem. In this context, the term ill-posed implies that the solution does not depend continuously on the data [5]. The process of achieving a balance between the fidelity and the stability of the solution is referred to as regularization, and is controlled by one or more regularization parameters [27]. These techniques often achieve this balance by incorporating a-priori information regarding the solution into the problem.

Implementation of the CLEAN algorithm involves a modification to the Van-Cittert algorithm (4.1), which allows for the selection of a single location in time and angle on each iteration where a signal arrival is likely to have occurred. This is appropriate in light of the fact that the problem at hand is essentially data detection rather than image restoration. The CLEAN algorithm is given as [19]

$$\mathbf{t}_{n+1} = \mathbf{t}_n + \gamma\overline{\max}\left(\mathbf{g} - \mathbf{D}\mathbf{t}_n\right) \tag{4.2}$$

where $\mathbf{t}_n$ is a LN element vector, formed by concatenating L beamformer look directions at N time instants, and is termed the *brightness distribution*, in analogy with the locations of sources in a radio astronomical map of the sky. The vector $\mathbf{g}$ also consists of LN elements, and represents the *dirty map,* or the beamformer response to the measured data. $\mathbf{D}$:$\mathbb{R}^{LN} \rightarrow \mathbb{R}^{LN}$ is an operator which maps the brightness distribution into the dirty map for each angle-of-incidence and look direction, over all time instants. The constant γ again represents the loop gain and is restricted to $0 < \gamma \leq 1$. The operator $\overline{\max}(\cdot)$: $\mathbb{R}^{LN} \rightarrow \mathbb{R}^{LN}$, returns the largest absolute element of the argument vector, at the location in the vector where it occurred, and zeroes elsewhere. The idea is to iteratively drive the residual term to zero by finding the brightness distribution which best approximates the actual location of signals impinging on the array, while allowing for errors in the estimation process to be iteratively corrected [10]. Here $\mathbf{D}$ is generally assumed to have a circulant structure, in order to represent the convolution of the brightness distribution with the point-spread function.

It is important to note that this algorithm is not linear, but rather is modeled as piecewise linear, at best [10]. If the observation space over time and look-angle is divided into N regions such that in the i^{th} region the residuals $|R_i|$ are due only to the signal $s_i(t)$, then the i^{th} linear iterative relaxation process can be proposed to reduce this residual. The difficulty is in the fact that piecewise linear iterations are not easily analyzed, and the asymptotic behavior cannot be proven [10]. Convergence of the CLEAN algorithm has been demonstrated [42], under the conditions that $0<\gamma \leq 1$ and the blurring matrix $\mathbf{D}$ is symmetric and positive definite or semi-definite.

Use of the $\overline{\max}(\cdot)$ operator in (4.2) can also be justified by instead applying the Van-Cittert algorithm (4.1) to the beamformer response to an incident signal. Then, starting with $\mathbf{t}_0 = \mathbf{0}$, the first iteration gives $\mathbf{t}_1 = \gamma\mathbf{g}$, a scaled replica of the dirty map. For the signal detection problem at hand, $\mathbf{t}_1$ contains all of the signals of interest as well as the undesired artifacts. The dynamic range of this iteration is therefore limited immediately by γ.

In the UWB case, the matrix $\mathbf{D}$ describes the beampattern or the beamformer response over time and angle to a signal waveform, which is a function of the incident pulse shape as shown in Chapter 3. Given the dynamics of the received signal, as seen in Figure 1-3, the CLEAN technique in equation (4.2), must be used in conjunction with a decomposition, such as that given in equation (A.7) of the Appendix, in order to model the indoor UWB channel. In other words, no single pulse shape appears to provide an accurate model for all of the incident signals. This then implies that multiple blurring matrices $\mathbf{D}$ will be required, one corresponding to each waveform in the basis of the decomposition. As discussed in the Appendix, however, use of a signal model such as the Hermite collection of pulses does not necessarily provide a robust solution. The problems with this basis for the decomposition of UWB signals include the lack of shift-orthogonality and the loss of orthogonality between different modes in the representation in the event of pulse dispersion or distortion. Thus, UWB sidelobe reduction and signal identification techniques based on these decompositions were not developed beyond this point. Further, there is no physical reason to expect the blurring matrix $\mathbf{D}$ to exhibit symmetry, given some transmitted pulse shape. This eliminates the previous analyses on the convergence of the CLEAN algorithm [43], [42] from applicability to this problem.

A modification to the CLEAN algorithm of equation (4.2) renders it more directly applicable to the problem at hand. Upon identification of the peak residual between the beamformer response to the measured data and the response to the recovered signals, the location in the data from *each sensor*, corresponding to the peak, is identified and the amplitude reduced by a factor of γ. The beampattern is then reformed from this adjusted data and the next peak located. This algorithm will be referred to as Sensor-CLEAN, since the relaxation step now takes place in the space of the sensor data, and can be described by the following equations

$$\begin{aligned} \mathbf{t}_{n+1} &= \mathbf{t}_n + \gamma \overrightarrow{\max} \left[\mathbf{B} \left(\mathbf{d} - \mathbf{w}_n \right) \right] &\quad (4.3) \\ \mathbf{w}_{n+1} &= \mathbf{w}_n + \gamma \mathbf{T}_r \left[\mathbf{B} \left(\mathbf{d} - \mathbf{w}_n \right) \right], &\quad (4.4) \end{aligned}$$

where $\mathbf{B} : \mathbb{R}^{MN} \to \mathbb{R}^{LN}$ represents the delay-and-sum beamformer as a linear operator, over M sensors, L look directions and N time instants. The MN element vector $\mathbf{d}$ contains the measured data, $\mathbf{w}_n$ represents the recovered sensor data at iteration n, and $\mathbf{T}_r : \mathbb{R}^{LN} \to \mathbb{R}^{MN}$ achieves the inverse mapping of the beamformer peak onto the sensor data, assuming a signal length of $2r + 1$ samples. The modified algorithm is shown in Figure 4-1.

The main difference between the CLEAN and Sensor-CLEAN is in the nature of the relaxation step, or the operation in which signals are identified and the amplitude is reduced by some

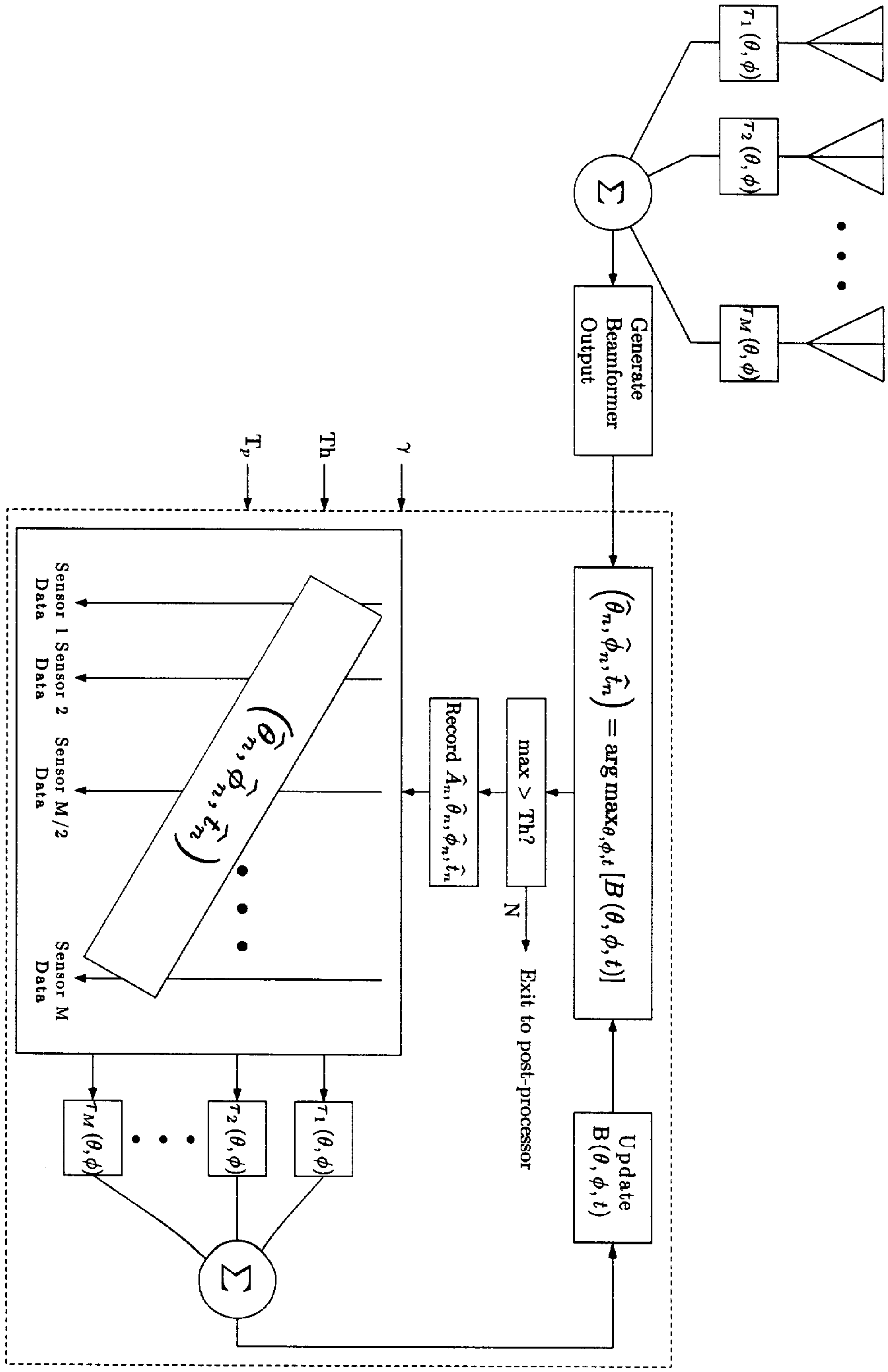

Figure 4-1: The Sensor-CLEAN algorithm

fraction. In the CLEAN algorithm, this relaxation step occurs in the space of the beamformer output, where in Sensor-CLEAN, the relaxation step is applied directly on the sensor data. This permits the operation to proceed with minimal assumptions on the shape of the received signal waveform, since it is not necessary to estimate the resulting beampattern precisely. The only a-priori information that is assumed is the impulsive nature of the incident signals; that the signal will have support in time of less than some maximum number of samples. Again, it is the sensor-to-sensor signal fluctuations present in the received UWB data which makes the beampatterns difficult to predict and hence difficult to regenerate based only on beam-space information. No information is lost in the fact that the relaxation step in now done in the space of the sensor data, instead of in beam-space, since the data processing inequality guarantees that the sensor data contains at least as much information as the beamformer output formed from this sensor data.

The Sensor-CLEAN algorithm requires three parameters to be set prior to initiating the iteration. Given that this is an indirect technique and not an exact solution to the problem, the results provided by the algorithm will be a function of these parameters. The loop gain term, denoted γ, is the fraction of the signal amplitude removed from the measured data during the relaxation step. The parameter T_p represents the maximum window in time (in samples) that the algorithm will process as a single arrival. This is where the strongest assumptions on the nature of the incident signals are made; that they are impulsive and will have support in time of less than $2T_p + 1$ samples. Finally, a detection threshold must be established, providing a condition for termination of the iteration.

Given the use of this algorithm, the following model for the response of the channel to a transmitted UWB signal can be discussed:

$$r(t) = \sum_{k=1}^{N} A_k s_k \left(t - \tau_k, \theta_k, \phi_k\right) + n(t), \tag{4.5}$$

where τ_k is the time-of-arrival of the k^{th} out of N signal components, at an azimuth angle of θ_k degrees and an elevation angle, measured from a perpendicular to the array, of ϕ_k degrees. The received impulse waveform, $s_k(t)$ depends on the index k, due to variations in the received signal shape. This dictates that, for each detected signal, the algorithm should estimate $s_k(t)$ from the received data, in addition to the time-of-arrival and angle-of-arrival.

The operation of the Sensor-CLEAN algorithm is shown in Figure 4-1 and is described in the following steps:

1. Collect the received signal data on an array of sensors, and generate the delay-and-sum beamformer output over a window in time and in azimuth and elevation arrival angle, according to

$$\mathbf{S} = \mathbf{Bd}, \tag{4.6}$$

   where $\mathbf{S}$ is the beamformer response to the sensor data, $\mathbf{B}$ represents the delay-and-sum beamformer and $\mathbf{d}$ is a vector of the measured data at each sensor, as before.

2. Search this beamformer output for the peak absolute component, recording the azimuth angle θ_0, elevation angle ϕ_0 and time-of-arrival t_0 of the peak, or

$$\{\theta_0, \phi_0, t_0\} = \arg\max \mathbf{S}. \tag{4.7}$$

3. Determine the location in the data from each sensor corresponding to the peak residual. Either use an a-priori hypothesis on the support in time of the incident signal, or determine the support of the incident signal by adjusting the window in each sensor over which the relaxation is conducted, and note the support which results in the minimum residual energy. The mapping of the beamformer peak location onto the sensor data is achieved by the operator $\mathbf{T}_r$ and the residual sensor components are then given by $\mathbf{T}_r\left[\mathbf{B}\left(\mathbf{d} - \mathbf{w}_n\right)\right]$ where $\mathbf{w}_n$ represents the recovered sensor data on the n^{th} iteration and $\mathbf{w}_0$ is an all zeros vector.

4. Reduce the residual on each sensor corresponding to the peak by a fraction γ, by adding the signal component to the recovered sensor data $\mathbf{w}_n$, according to equation (4.4).

5. Regenerate the residual beamformer output over the affected range in time and angle, according to $\mathbf{B}\left(\mathbf{d} - \mathbf{w}_n\right)$.

6. Search again for the largest residual value in the beamformer output map, given on the n^{th} iteration by

$$\{\theta_n, \phi_n, t_0\} = \arg\max\left[\mathbf{B}\left(\mathbf{d} - \mathbf{w}_n\right)\right], \tag{4.8}$$

where $\mathbf{w}_n$ represents the recovered sensor data, as above. If the resulting peak is above the detection threshold, then update the recovered signal information according to according to equation (4.3) and continue with step 3, else terminate the iteration.

7. When all residuals have been liquidated, or no signal components remain with amplitude greater than the detection threshold, accumulate the signal information collected during the iteration, and generate the associated main beams. Add this to the residual noise floor left over from the iteration,

$$\mathbf{S}_c = \mathbf{B}'\mathbf{w}_J + \mathbf{B}\left(\mathbf{d} - \mathbf{w}_J\right), \tag{4.9}$$

where the iteration was terminated on the J^{th} iteration, $\mathbf{S}_c$ represents the "clean" map and $\mathbf{B}'$ is an operator which generates the mainbeams of the detected signals only.

8. Post-process the Sensor-CLEAN output, $\mathbf{S}_c$, to determine the signal arrival information from this "clean" map, in the absence of the sidelobes. This operation will be discussed in greater detail shortly.

A few remarks on the algorithm are in order. First, convergence of the Sensor-CLEAN algorithm is guaranteed through a monotonic reduction in the residual energy on each iteration. The residual energy, as well as the peak residual, is smaller on each iteration than on the last, which insures that the algorithm will converge to some solution. This is demonstrated in Section 4.2, which discusses the optimality of the Sensor-CLEAN algorithm. As with most indirect algorithms, however, the solution generated by the Sensor-CLEAN algorithm is a function not only of the data, but of the input parameters as well. Thus the solution is not unique, and the parameters must be selected based on some criterion which generally trades estimate fidelity against computation time. For example, the quality of the estimates and the required computation time are inversely proportional to the loop gain γ and the relaxation window size, for a fixed detection threshold. This implies that some knowledge or judgement, possibly in the absence of an applicable theory for selection of values, must be applied in the determination of these parameters. Note that all randomness is contained in the data and not the algorithm; for fixed parameter values and data, the Sensor-CLEAN algorithm will return consistent results.

4.1.1 Post-processing of Sensor-CLEAN information - The Wave-Map Algorithm

The output of the Sensor-CLEAN algorithm consists of a list $\{a_n, \theta_n, \phi_n, t_n, \mathbf{w}_n\}_{n=1}^{N}$ of the amplitude a_n, the azimuth look direction θ_n, the elevation look direction ϕ_n, the time-of-arrival, t_n and the waveforms $\mathbf{w}_n$ recovered on each iteration. The algorithm also records the residual noise floor which remains after all components above the detection threshold have been removed. Because all signal detections corresponding to a single incident signal may not occur at precisely the same location in time and angle, resulting in multiple detections of the same signal at distinct locations, this list of arrivals must be further processed in order to more accurately estimate the signal parameters. A post-processing algorithm is therefore applied to the data, which takes into account the known spatio-temporal resolution limits of the UWB beamformer, and attempts to combine multiple detections which likely correspond to a single signal. These results form an initial estimate of the signal parameters. Since each hypothesized signal can now be considered in the absence of other signals which may have biased the initial estimates, an attempt is made next to re-estimate parameters of each detected signal, comparing each signal with the original beamformer output.

The first of two post-processing algorithms introduced in this work is referred to as the Wave-Map algorithm, and is shown in Figure 4-2. In this routine, the mainbeams corresponding to each of the detections reported by the Sensor-CLEAN algorithm are formed, and added onto the residual output map, denoted in the figure by $\mathbf{R}(t_n, \theta_n, \phi_n)$. This composite map is then searched and the maximum value is recorded. If this maximum is greater than the detection threshold, then all elements in the list, $\{a_n, \theta_n, \phi_n, t_n, \mathbf{w}_n\}_{n=1}^{N}$, that are within a distance T_w seconds in time and Θ_w degrees in azimuth angle of the maximum are marked as detected, and removed from further consideration. The parameters T_w and Θ_w are chosen to reflect the spatio-temporal resolution limit of the UWB array and beamformer. The mainbeams associated with all remaining undetected elements of the arrival list are then formed and added to the residual map. This process repeats until the detection threshold is no longer satisfied.

When the formation of the mainbeams from the undetected arrivals results in no components in the output map with value greater than the detection threshold, the iteration terminates and a re-estimation routine is applied. This routine compares the recovered signal amplitude, time-of-arrival and angle-of-arrival against the original measured data, and adjusts the recovered signal data to more accurately reflect the measured data, when necessary. The parameters required to accomplish this are the one-sided time window, T_{re}, azimuth angular window, Θ_{re}, and the elevation angular window, Φ_{re}, over which to search. The re-estimation procedure then generates the beamformer output from the measured data in a window around the detected arrival. This window is then searched for the maximum value, which is then reported as the final location in time and angle of the incident signal.

4.2 Optimality of the Sensor-CLEAN Algorithm

If the assumptions are made that the beampatterns associated with different pulses do not interfere, as defined below in equation (4.13), and that all of the incident pulses have equal energy, then the Sensor-CLEAN algorithm is optimal in that for fixed parameters, it generates the solution with minimum residual energy. This can be seen as follows. First, define the residual energy on iteration j as equal to

$$R_j = \sum_{n=0}^{N-1} \sum_{m=0}^{L-1} |B_j(n,m)|^2, \tag{4.10}$$

where $B_j(n,m) = \mathbf{B}(\mathbf{d} - \mathbf{w}_j)$ represents the residual beamformer output map at iteration j over N time samples and L look directions, as in equation (4.3) and equation (4.3). The initial output map can be modeled by considering the superposition of the incident pulses and their beampatterns,